Mechanisms Governing Target Search and Binding Dynamics of Hypoxia-Inducible Factors

Yu Chen[1,2,3], Claudia Cattoglio[1,2,3], Gina Dailey[1,3], Qiulin Zhu[1,3], Robert Tjian[1,2,3] *, and Xavier Darzacq[1,3] *

[1] Department of Molecular and Cell Biology, University of California, Berkeley, CA, USA.
[2] Howard Hughes Medical Institute, University of California, Berkeley, CA, USA.
[3] Li Ka Shing Center for Biomedical & Health Sciences, University of California, Berkeley, CA, USA.

*Correspondence: R.T. (jmlim@berkeley.edu), X.D. (darzacq@berkeley.edu)

Abstract

Transcription factors (TFs) are classically attributed a modular construction, containing well-structured sequence specific DNA-binding domains (DBDs) paired with disordered activation domains (ADs) responsible for protein-protein interactions targeting cofactors or the core transcription initiation machinery. However, this simple division of labor model struggles to explain why TFs with identical DNA binding sequence specificity determined *in vitro* exhibit distinct binding profiles *in vivo*. The family of Hypoxia-Inducible Factors (HIFs) offer a stark example: aberrantly expressed in several cancer types, HIF-1α and HIF-2α subunit isoforms recognize the same DNA motif *in vitro* – the hypoxia response element (HRE) – but only share a subset of their target genes *in vivo*, while eliciting contrasting effects on cancer development and progression under certain circumstances. To probe the mechanisms mediating isoform-specific gene regulation, we used live cell single particle tracking (SPT) to investigate HIF nuclear dynamics and how they change upon genetic perturbation or drug treatment. We found that HIF-α subunits and their dimerization partner HIF-1β exhibit distinct diffusion and binding characteristics that are exquisitely sensitive to concentration and subunit stoichiometry. Using domain-swap variants, mutations, and a HIF-2α specific inhibitor, we found that although the DBD and dimerization domains are important, a major determinant of chromatin binding and diffusion behavior is the AD-containing intrinsically disordered region (IDR). Using Cut&Run and RNA-seq as orthogonal genomic approaches we also confirmed IDR-dependent binding and activation of a specific subset of HIF-target genes. These findings reveal a previously unappreciated role of IDRs in

34 regulating the TF search and binding process that contribute to functional target site selectivity on
35 chromatin.

Introduction

Sequence-specific transcription factors (TFs) are key frontline regulators of gene expression. Classical LexA-Gal4 domain-swap experiments in yeast presented a simple modular structure and apparent division of labor for typical TFs (Brent and Ptashne, 1985). In this textbook paradigm, the DNA-binding domain (DBD) is responsible for DNA sequence recognition and binding specificity while the activation domain (AD) is responsible for target gene transactivation that involves protein-protein interactions with co-factors, the basal transcription machinery and other ancillary factors that are generally devoid of sequence specific DNA recognition. In higher eukaryotes, each DBD class usually contains multiple closely related family members. For example, the bHLH class of TFs includes MyoD, Clock, and Max. They all recognize the same E-box DNA binding sequence motif 5'-CACGTG-3', yet each differentially regulates muscle differentiation, circadian rhythm, and cell proliferation, respectively (Kribelbauer et al., 2019). This raises the specificity paradox: how do TFs with seemingly identical DNA sequence specificity, at least as determined *in vitro*, nevertheless exhibit non-overlapping binding profiles *in vivo* and carry out distinct and even opposing functions? In general, when confronted with this conundrum, we have assumed that one or more co-factors or perhaps still to be identified "silent partner" TFs can somehow divert target recognition to a composite cis-regulatory site distinct from the canonical DNA binding site. Given the high occurrence of short binding motifs for most TFs throughout the genome, even with co-operative binding to composite sites, most potential specific binding sites nevertheless remain unoccupied as determined by genome-wide TF binding studies. What feature or motif within TFs outside of the DBD and dimerization domain may be responsible for such differential site selection has remained unclear. Thus, the simple rule of modular units with well separated divisions of labor between DBD, dimerization and transactivation may deserve a closer look. We also wondered whether quantitative single molecule dynamics measurements might reveal new aspects of TF behavior in living cells that could inform us regarding potential mechanisms influencing the target search and binding process and differential site selectivity in a native physiologically relevant context.

Here we have chosen the Hypoxia-Inducible Factors (HIFs) as a representative example to study the paradox of highly conserved DBDs carrying out distinct target site selection and to dissect potential novel features of TFs that mediate chromatin binding. HIFs are a family of α/β heterodimeric TFs stabilized under hypoxic conditions to promote angiogenesis, anaerobic metabolism, cell proliferation and "stemness" (Semenza, 2012). The oxygen-labile alpha subunits (mainly HIF-1α and HIF-2α) complex with their oxygen-stable beta partner (mainly HIF-1β) to form

70 a functional dimer (Figure 1A). All HIF subunit isoforms belong to the bHLH-PAS (Basic helix-
71 loop-helix-PER-ARNT-SIM) family, where the N-termini are structured domains containing bHLH
72 (DNA binding) and PAS (dimerization) domains, while the C-termini consist of intrinsically
73 disordered regions (IDRs) containing ADs (Figure 1A; Figure 1—figure supplement 1A). HIF-
74 1α/1β and HIF-2α/1β dimers share a conserved structural fold (Wu et al., 2015), recognize the
75 same hypoxia response element (HRE) 5'-TACGTG-3' binding motif (Schödel et al., 2011;
76 Wenger et al., 2005), but share only a partial overlap of target genes *in vivo* (Smythies et al.,
77 2019). With their own unique target gene sets, HIF-1α and -2α can exert divergent and even
78 contrasting functions (Keith et al., 2012). For example, while both HIF-1α and HIF-2α regulate
79 angiogenesis, HIF-1α specifically regulates glycolysis, apoptosis, and promotes NO production,
80 whereas HIF-2α binds to the *POU5F1* locus to maintain Oct4-regulated stem cell identity and
81 pluripotency, promotes cell cycle progression, and inhibits NO production (Keith et al., 2012, p. 1;
82 Smythies et al., 2019). Therefore, our current simple textbook model of exchangeable modular
83 TF functional units does not satisfactorily explain such isoform-specific target gene regulation.
84
85 The HIF family differential specificity paradox is even more daunting to comprehend at the level
86 of disease inducing mechanisms. HIFs are aberrantly upregulated and recognized as oncogenic
87 drivers in multiple cancers. However, in addition to their shared roles in cancer onset and
88 progression, HIF-1α and -2α also show many independent, sometimes even opposing roles in
89 specific contexts (Keith et al., 2012). For example, in clear cell renal cell carcinoma (ccRCC), HIF-
90 2α is the critical tumorigenic driver whereas HIF-1α, in contrast with its usual tumorigenic role, is
91 mostly tumor-suppressive (Raval et al., 2005; Schödel et al., 2016). The regulatory mechanism
92 behind such highly divergent outcomes is still largely unknown. Given such complexity, without a
93 deeper understanding of isoform-specific transcriptional regulation, it is hard to predict the
94 functional outcomes mediated by individual HIF isoforms in various cancer types or stages, which
95 could be a complicating factor in developing more effective HIF-targeting cancer therapeutics.
96
97 In this study, we aim to understand the molecular mechanisms mediating isoform-specific target
98 gene regulation at its most fundamental level – could we detect differential molecular dynamics
99 of distinct TF isoforms during the target search and chromatin binding process in live cells? Which
100 regions or domains of TFs might be responsible for such isoform specific properties? Could we
101 begin to discern possible mechanisms that guide TFs with highly conserved DBDs to their distinct
102 and specific targets beyond cognate DNA sequence recognition? Here we use HIFs as an
103 illustrative example, combining endogenous tagging and super-resolution single particle tracking

104 (SPT) (Liu et al., 2015) to study the dynamic behavior of these key gene regulators in live cells
105 under physiological conditions. We also dissect the contribution of different domains of HIF-α
106 isoforms by a series of mutation and domain swap experiments to directly test the concept of
107 modular functional domains. Deploying a combination of genetic and small-molecule
108 perturbations, we found that, although HIF DBD and dimerization are important for DNA target
109 acquisition, the amount of protein bound and its diffusion characteristics are mainly driven by
110 regions outside the DBD and dimerization domains. Finally, using genomic approaches we found
111 that, in concordance with our imaging results, binding strength and gene activation are IDR-
112 dependent for a subset of HIF target sites. Our results reveal a previously unappreciated role of
113 unstructured domains in the target search and binding properties of TFs to functional chromatin
114 sites in a live cancer cell context.
115
116 **Results**
117
118 **Establishing a human cancer cell system for live-cell single molecule imaging of HIF**
119 To investigate HIF dynamics, we first focused on one of the cognate dimers: HIF-2α/1β. We used
120 the common ccRCC line 786-O (Brodaczewska et al., 2016), derived from a VHL-deficient, H2
121 type primary clear cell renal cell carcinoma, wherein HIF-2α is stabilized due to an inactivating
122 mutation in VHL (the E3 ubiquitin ligase that targets all HIF-α isoforms for proteasomal
123 degradation)(Gnarra et al., 1994). The 786-O line also conveniently lacks any functional HIF-1α
124 due to a truncating mutation of HIF-1α (Shen et al., 2011; Swiatek et al., 2020, p.), which allows
125 us to study one α isoform independently from the other. Using CRISPR/Cas9-mediated genome
126 editing, we successfully generated several clonal lines with homozygous knock-in (KIN) of the
127 HaloTag (Los et al., 2008) at the N-terminus of either HIF-2α or its binding partner, HIF-1β (Figure
128 1B; Figure 1—figure supplement 2). Western blotting confirmed that the tagged proteins are
129 expressed at levels similar to wild-type (WT) in unedited cells (e.g., HIF-2α clone A31 and HIF-
130 1β clone A21) (Figure 1B). Confocal imaging after covalently labeling cells with a fluorescent
131 Halo-binding ligand (JFX646) (Grimm et al., 2021) shows the expected nuclear localization for
132 both Halo-HIF-2α and Halo-HIF-1β proteins (Figure 1C). In addition, we confirmed by ChIP-seq
133 that both tagged proteins maintain a similar genome-wide binding profile as the WT protein in
134 unedited cells (Figure 1—figure supplement 3A), and RNA-seq confirmed that gene expression
135 profiles in both edited cell lines are not significantly altered from WT unedited cells (Figure 1—
136 figure supplement 3B-C, with cells overexpressing WT and mutant HIF-α as controls). We have

137 thus established a human cancer cell system suitable for live-cell imaging of HIF-2α and HIF-1β
138 at endogenous expression levels.
139
140 To evaluate how HIF-2α and -1β explore the nucleus and bind DNA, we used the fast modality of
141 super resolution live cell single particle tracking (fSPT) that is capable of tracking rapidly diffusing
142 molecules. Cells with either HIF-2α or HIF-1β Halo KIN were doubly labeled with the live-cell
143 permeable Halo-binding JFX dyes (Figure 1D) and were imaged under highly inclined and
144 laminated optical sheet illumination (HiLo) (Tokunaga et al., 2008) at high frame rates (~182 Hz)
145 to capture the movement of single molecules in their native nuclear environment (Figure 1E).
146 Stroboscopic illumination at high excitation power is used to minimize motion blur, while sparse
147 labeling ensures only a limited number of molecules are detected at any given time in the nucleus
148 to minimize misconnections when computing the path of individual molecules (trajectories) (Figure
149 1E-F). We can then estimate relevant kinetic parameters from these trajectories, extracting
150 quantitative information such as diffusion coefficients and bound fraction.
151
152 **fSPT detects various HIF molecular states in their native nuclear environment**
153 To quantitatively analyze the acquired fSPT data, we used a non-parametric Bayesian "state array"
154 (SA) approach (Heckert et al., 2021) recently developed in our lab. Briefly, SA analyzes regular
155 Brownian motion with normally distributed localization error (RBME) with a two-dimensional "grid
156 of states" that spans a range of diffusion coefficients (first dimension) and localization error
157 (second dimension) magnitudes, and evaluates the occupancy (proportion) of each state in this
158 array using the observed fSPT trajectory data and a variational Bayesian algorithm. After
159 inference, the proportion of molecules as a function of diffusion coefficient is calculated by
160 marginalizing localization error, creating a "diffusion spectrum" that reports the underlying
161 molecular subpopulations according to their proportions (y-axis) and their diffusive properties
162 (diffusion coefficients, x-axis) (Figure 2—figure supplement 1). While our previous approach
163 required the assumption of a fixed and limited (3 or less) number of states for the tracked protein
164 (Hansen et al., 2018), this SA approach does not require *a priori* knowledge or any assumption
165 regarding the number of subpopulations or "states" of the tracked molecules. Also, it is more
166 robust for fSPT trajectories as it accounts for known experimental biases due to localization error
167 and fluorophore defocalization (Heckert et al., 2021). We chose to use this new method, because
168 as dimeric transcription factors, HIF subunits could conceivably exist in many states (e.g., bound,
169 moving as a monomer, moving as a dimer, and moving in a bigger complex containing co-

170 regulators) (Figure 2A-B) and the SA approach better suits our needs for model-free analysis
171 without assuming any given number of states.
172
173 We first analyzed individual cells to check cell-to-cell variation. Due to the small number of
174 trajectories per cell, we used a less precise version of the SA calculation, the "naïve occupation
175 estimate" by simply applying the RBME likelihood estimation to individual cells without refining
176 the posterior over diffusion coefficient and localization error (Figure 2—figure supplement 1A-B,
177 top) (Heckert et al., 2021). We observed rather heterogeneous results for both HIF-2α and HIF-
178 1β, with varied diffusion coefficient estimates from cell to cell (Figure 2A-B; Figure 2—figure
179 supplement 2A, clones A31 and A21). While the heterogeneity we observed was likely due to the
180 limited number of trajectories collected from each cell (i.e. small sample bias) rather than to a
181 difference in behavior of HIF proteins in each cell, our findings do indicate that a range of moving
182 states likely exists for both HIF proteins.
183
184 We then pooled trajectories from many cells (n ~60 from 3 biological replicates for each
185 experimental condition) to estimate the distribution of diffusion coefficients for the population. SA
186 generates a distribution of diffusion coefficient estimates that reports the fraction of stably bound
187 molecules while simultaneously displaying the full behavioral spectrum of the diffusing molecules
188 (Figure 2C; Figure 2—figure supplement 1A-B, bottom). We define the fraction with a diffusion
189 coefficient < 0.1 μm^2/sec as immobile and presumably chromatin-bound (see Figure 2—figure
190 supplement 3 and Appendix 1 for discussion of source of variations between replicates). Strikingly,
191 we observed a very different behavior for Halo-HIF-2α compared to Halo-HIF-1β. Whereas a large
192 fraction (about 40%) of Halo-HIF-2α is bound, the majority (above 70%) of Halo-HIF-1β appears
193 freely diffusing (Figure 2C; Figure 2—figure supplement 2B, clones A31 and A21). Also, the
194 overall diffusion coefficient for the Halo-HIF-1β mobile population is much larger than that of Halo-
195 HIF-2α. We repeated measurements in different KIN clones and confirmed the reproducibility of
196 these results for both Halo-HIF-2α (Figure 2—figure supplement 2A-B, clone B50) and Halo-HIF-
197 1β (Figure 2—figure supplement 2A-B, clone B89). Note that although we quantitatively compared
198 the bound fraction, due to the complexity of the composition of the moving population (i.e. multiple
199 states might exist but are merged into a single peak), quantitatively comparing mode (i.e. peak)
200 or mean diffusion coefficient may give slightly different results. Therefore, for the rest of the paper
201 we only present the peak diffusion coefficient in the figures but listed both peak diffusion
202 coefficient and mean diffusion coefficient for the moving population in Table 1.
203

204 The differences between HIF-2α and -1β seem counterintuitive at first, because one would expect
205 HIF-2α and HIF-1β to behave similarly since they should exist as a hetero-dimer. However, since
206 the endogenous HIF-1β is expressed at a much higher level than HIF-2α (Figure 1—figure
207 supplement 2C), the majority of HIF-1β is likely free to diffuse without HIF-2α. Of note, the
208 distribution plot only reflects the fraction of molecules as a function of their diffusion coefficient,
209 but does not report on the absolute number of molecules. Therefore, a smaller bound fraction for
210 Halo-HIF-1β does not mean fewer numbers of bound molecules than Halo-HIF-2α, since many
211 more Halo-HIF-1β molecules are present in the nucleus. Given this scenario, we hypothesized
212 that HIF-1β molecular dynamics and percent binding should be modulated by changing the 2α/1β
213 stoichiometry.
214
215 **HIF-1β binding and diffusing dynamics can be modulated by HIF-α:β stoichiometry, and**
216 **are dependent on dimerization**
217 To test the hypothesis that HIF-1β dynamics depends on 2α/1β ratio, we first tried to modulate its
218 behavior by stably over-expressing HIF-2α in the endogenously HIF-1β Halo-tagged KIN line
219 (Figure 2D). We found that the mobile population of Halo-HIF-1β diffuses more slowly when HIF-
220 2α is overexpressed, most likely due to its dimerization with the extra HIF-2α to form dimers
221 capable of DNA/chromatin binding. As expected, we also observed a significant increase in the
222 Halo-HIF-1β bound fraction (up to 50%), (Figure 2E; Figure 2—figure supplement 2C, top and
223 middle). To confirm that the changes in HIF-1β dynamics caused by increasing levels of HIF-2α
224 are dependent on hetero-dimerization, we stably overexpressed the HIF-2α R171A/V192D double
225 mutant (HIF-2α DM) that was previously reported to lose its dimerization capability with HIF-1β
226 (Wu et al., 2015). As expected, overexpression of HIF-2α DM did not increase the bound fraction
227 or decrease the overall diffusion coefficient of Halo-HIF-1β to the same extent seen with WT HIF-
228 2α overexpression (Figure 2E; Figure 2—figure supplement 2C, bottom), suggesting that the
229 changes we observe are dimerization-dependent.
230
231 We further validated our results by stably overexpressing different forms of HIF-α in the HIF-1β
232 Halo-tagged KIN line and treating cells with a HIF-2α-specific small molecule inhibitor, Belzutifan
233 (PT-2977). Belzutifan inhibits HIF-2α/1β, but not HIF-1α/1β, dimerization by specifically binding
234 to the dimerization domain of HIF-2α (Figure 3—figure supplement 1A), and thus has been used
235 as an HIF-2α inhibitor for ccRCC treatment (Wallace et al., 2016; Xu et al., 2019). We first
236 confirmed that Belzutifan inhibits HIF-2α transcription function in a dose-dependent manner
237 (Figure 3—figure supplement 1B). Importantly, Belzutifan also reduces the HIF-2α bound fraction

238 in the HIF-2α Halo-tagged KIN line in a similar dosage-dependent manner, again revealing the
239 potential of fSPT to measure TF dynamics and associated functional changes (Figure 3—figure
240 supplement 1C-E). We choose to use 0.2 μM Belzutifan for all subsequent experiments to
241 maximize its effect.
242
243 Next, we carried out a series of experiments designed to probe the consequences of swapping
244 different functional domains of HIF-1α and HIF-2α to determine which parts of these closely
245 related TFs might be involved in selective activities when paired with HIF-1β. Using the HIF-1β
246 Halo-tagged KIN line as the parental line, we stably overexpressed WT or chimeric HIF-α, where
247 we swapped the structured and disordered domains between HIF-1α and HIF-2α (Figure 3A). All
248 these different HIF-α variants are expressed from a relatively strong EF-1alpha promoter and are
249 N-terminally 3xFLAG-tagged. A construct that expresses 3xFLAG only is used as control. We
250 then treated these cells with either Belzutifan or DMSO control and measured Halo-HIF-1β
251 dynamics (Figure 3A). While 3xFLAG tag had no effect, overexpressing HIF-α, regardless of
252 which variant form, is able to both increase the bound fraction and reduce the overall diffusion
253 coefficient of HIF-1β (Figure 3B, top, and 3C, DMSO group). For cells overexpressing the α
254 variants that contain the HIF-2α structured domain, this effect on HIF-1β can be at least partially
255 reverted after Belzutifan treatment (Figure 3B-C, +HIF-2α and +HIF-2α/1α). In contrast, for cells
256 overexpressing the α variants that contain the HIF-1α structured domain, this effect is resistant to
257 Belzutifan, consistent with the subunit isoform specificity of the drug for HIF-2α (Figure 3B-C,
258 +HIF-1α and +HIF-1α/2α). In untransfected and 3xFLAG only overexpressing control cells,
259 treatment with Belzutifan only weakly reduces the HIF-1β bound fraction, again suggesting that
260 the majority of HIF-1β is not engaged with 2α (Figure 3B-C, parental cell and +3xF). Overall, these
261 results demonstrate that HIF-1β dynamics change after engagement with its α partner and can
262 be selectively inhibited with a specific dimerization inhibitor. The observed differences also
263 confirm that fSPT is a powerful platform to monitor molecular dynamic changes of TFs in living
264 cells thus, allowing us to gain new mechanistic insights while we introduce various perturbations,
265 such as subunit concentration or stoichiometry and specific mutations.
266
267 **Regions outside the DBD/dimerization domain determine HIF molecular dynamics**
268 Interestingly, comparing the effects of the four different α variants, we found that regardless of
269 their structured domain, those with the same C terminal IDRs behave similarly (Figure 3B-C,
270 middle and right). Specifically, the variants containing the HIF-2α IDR have a stronger effect on
271 increasing HIF-1β binding than the variants containing the HIF-1α IDR. Thus, surprisingly, it

272 appears that the bound fraction of HIF-1β is not determined by the HIF-α DBD, but rather by HIF-
273 α IDR, which we found rather counterintuitive. To confirm the importance of HIF-α IDRs in HIF
274 binding, we overexpressed a truncated version of either HIF-1α or -2α that contains only the N-
275 terminal structured region (HIF-1α NT or HIF-2α NT), which still maintains both the DBD and
276 dimerization capability for interacting with HIF-1β (Wu et al., 2015). Indeed, both these truncated
277 forms lacking the IDR/AD of HIF-α minimally affect the HIF-1β bound fraction (Figure 3—figure
278 supplement 2). Surprisingly, these truncated HIF-α variants also only marginally influenced the
279 overall HIF-1β diffusion coefficient. These results indicate that dimerization alone neither
280 increases HIF-1β binding nor reduces the overall diffusion coefficient of its moving population.
281 Instead, the extended HIF-α AD-containing IDR appears necessary to influence and direct HIF-
282 1β behavior.
283
284 To further test our hypothesis that HIF chromatin binding and the dynamics of the diffusion
285 population are dominated by the α subunit IDR, we switched to image the α subunit itself. We
286 made different forms of Halo-tagged HIF-α (WT and domain-swapped), stably but weakly
287 expressed them in WT 786-O cells with an L30 promoter (Figure 4A). To minimize differences in
288 expression levels among different HIF-α forms, we selected cells with a roughly similar
289 fluorescence intensity in the "cell-picking channel" (Figure 1D, left). Later we verified that the
290 movies captured in the "fSPT tracking channel" (Figure 1D, right) have similar localization density
291 in the initial 10 frames (Figure 4—figure supplement 1; see also Appendix 2 for full discussion).
292 We confirmed that when controlled for similar expression levels, binding and diffusion
293 characteristics of L30-expressed Halo-HIF-2α are very similar to the endogenous Halo-HIF-2α in
294 the KIN line (Figure 4—figure supplement 2), demonstrating that weak overexpression can largely
295 recapitulate endogenous protein behavior. Therefore, this system provides a convenient tool to
296 investigate the contribution of each domain of HIF-α in the target search and binding process.
297
298 Much like our results with endogenous HIF-1β, we observed similar behaviors of HIF-α proteins
299 if they contain the same IDR (Figure 4B, top and middle), while displaying distinct behaviors when
300 endowed with different IDR isoforms (Figure 4B, bottom). Regardless of which DBD they have,
301 the variants containing the HIF-2α IDR (WT HIF-2α and HIF-1α/2α) show a higher bound fraction,
302 compared to the ones containing HIF-1α IDR (WT HIF-1α and HIF-2α/1α) (Figure 4C). These
303 results suggest that indeed the disordered region on HIF-α determines how HIFs bind and diffuse
304 in the nucleus, and that the HIF-2α AD-containing IDR mediates more or stronger binding to
305 chromatin and/or some other relatively immobile components in 786-O cells.

306

307 **HIF-α disordered region is necessary but not sufficient for optimal binding**

308 The fact that the extent of binding (presumably to chromatin) of HIF proteins depends mainly on
309 the long C-terminal IDR rather than on their DBD was unexpected. Therefore, we next examined
310 the contribution of the HIF DBD to the bound fraction. We introduced point mutations in the DBD
311 (HIF-2α R27E and HIF-1α R30E) that were previously reported to impair DNA binding (Michel et
312 al., 2002; Wu et al., 2015), and expressed them in the WT 786-O cells with the same L30 promoter
313 system (Figure 5A). Not surprisingly, DBD mutants show a reduction in the bound fraction and a
314 concomitant increase in the diffusing fraction compared to their WT counterpart (Figure 5B-C). In
315 agreement with the expectation that the DBD mutations should not perturb protein-protein
316 interactions, we do not observe a significant change in the overall diffusion coefficient of the
317 moving population. These results demonstrate that, although the AD-containing IDR is the major
318 modulator in determining the differences in bound fraction among different HIF dimers, the DBD
319 is also important for binding, further suggesting that the observed bound fraction likely represents
320 chromatin/DNA binding.

321

322 We next examined whether dimerization with HIF-1β is required for HIF-α chromatin binding.
323 Taking advantage of the same L30 weak expression system, we exogenously expressed the
324 Halo-HIF-2α dimerization mutant (R171A/V192D), or the analogous Halo-HIF-1α dimerization
325 mutant (R170A/V191D) in the WT 786-O cells (Figure 5D). We found that compared to the WT
326 Halo-HIF-2α or -1α, these mutants exhibit a significantly decreased bound fraction (Figure 5E-F),
327 demonstrating that HIF-α without -1β can no longer effectively bind to DNA/chromatin. Taken
328 together, our results indicate that the HIF-α disordered region alone is not sufficient to maintain
329 binding, but instead, the IDR and both the DBD and dimerization domains are also needed.

330

331 **Intrinsic properties of HIF-α IDR determine the overall rate of diffusive HIF.**

332 Interestingly, with the Halo-HIF-α dimerization mutants, we observed no obvious change in their
333 overall diffusion coefficient in the moving population (Figure 5E-F; Table 1), indicating that losing
334 their HIF-1β partner does not affect the overall HIF-α diffusion rate. This result suggests that it is
335 some intrinsic property of HIF-α molecules, rather than the molecular weight of dimers versus
336 monomers, that determines its diffusion rate and behavior. Our results suggest that while the
337 moving population of HIF-1β alone diffuses relatively fast, the moving population of both HIF-α
338 and HIF- α/β dimers diffuses relatively slowly. We postulate this is potentially due to the HIF-α
339 IDR engaging in protein-protein interactions with various cofactors both when associated with

340 HIF-1β or when alone (Figure 8A). Indeed, this is consistent with our previous observation that
341 the HIF-a NT/HIF-1β dimer diffuses at a relatively fast rate, similar to HIF-1β alone which
342 apparently does not share this HIF-α IDR mediated capacity (Figure 3—figure supplement 2).
343
344 **HIF-α IDR contributes to binding preferences and regulatory specificity of target genes.**
345 To see how differences in HIF molecular dynamics relate to actual genome-wide binding, we
346 performed Cut&Run on 786-O cells stably expressing different forms of Halo-tagged HIF-α driven
347 by the L30 promoter (same cells we performed fSPT on in Figure 4). All these exogenously
348 expressed proteins contain a V5 tag at the N-terminus of the Halo-tag, which we used as the
349 epitope for Cut&Run antibody recognition. The Halo-HIF-2α KIN clone A31 served both as a
350 positive control and as a reference for endogenous HIF-2α binding, as it also contains a V5 tag
351 N-terminal to the Halo-tag. WT cells without genetic modification controlled for V5 antibody non-
352 specific binding. Interestingly, the overall genome-wide binding profiles are very similar for all HIF-
353 α variants we examined (Figure 6—figure supplement 1), where most of the endogenous HIF-2α
354 binding sites are also bound by all exogenously expressed HIF-α (-1α, -1α/2α, -2α, and -2α/1α).
355 Even genes that are known to be regulated by one or the other isoform (e.g, the HIF-1α responsive
356 gene *PGK1* and the HIF-2α responsive gene *TGFA* (Keith et al., 2012)) are bound by all α forms
357 at their promoters/enhancers.
358
359 However, we did find significant differential binding preferences dictated by the IDR at a subset
360 of HIF target sites (Figure 6A-B; Figure 6—figure supplement 2). For example, the enhancer of
361 HIF-2α responsive genes such as *HSD3B7* and *PLXNA2* show increased HIF-2α binding when
362 cells are expressing extra HIF-2α, but no change in HIF-1α binding when HIF-1α is overexpressed.
363 Interestingly, such an increase in binding is also seen when overexpressing HIF-1α/2α, but not
364 the HIF-2α/1α chimera and, importantly, results in selective gene activation (Figure 6B; Figure
365 6—figure supplement 2B). The opposite is true for the HIF-1α responsive *PPFIA4* promoter and
366 *PTPRN* enhancer (Figure 6A; Figure 6—figure supplement 2A): a specific increase in HIF-1α and
367 HIF-2α/1α binding selectively induces both genes, which are instead insensitive to elevated HIF-
368 2α and HIF-1α/2α levels. These genome-wide analyses confirm that IDR-guided binding by HIF-
369 2α versus HIF-1α can indeed differentially activate selected gene loci.
370
371 Because IDR-specific binding is not readily detectable at a genome-wide scale due to the intrinsic
372 limitations of ensemble measurements, we next focused on differentially regulated sites only. We
373 first identified sites that respond differentially to either HIF-1α or HIF-2α, and then ask what is the

binding signal strength for the HIF-1α/2α and HIF-2α/1α chimeras - do they resemble more those of HIF-1α or HIF-2α, depending on their DBD or IDR (Figure 6C)? We define sites that show elevated binding only when HIF-1α is overexpressed as HIF-1α responsive (Table 2), and sites that show elevated binding only when HIF-2α is overexpressed as HIF-2α responsive (Table 3). For HIF-1α responsive regions, we observed elevated binding when overexpressing either HIF-1α/2α or HIF-2α/1α, compared to HIF-2α, indicating that HIF-1α DBD and IDR both contribute binding to HIF-1α responsive regions. For HIF-2α responsive regions, binding tended to be more elevated for HIF-1α/2α compared to HIF-2α/1α, suggesting that HIF-2α IDR might dominate binding to HIF-2α responsive sites (Figure 6C; Figure 6—figure supplement 3).

Unlike Cut&Run data, we observe clear genome-wide IDR-dependent gene regulation for RNA-seq performed on the same sets of cells. Specifically, cells overexpressing the HIF variants containing the same IDR show similar overall gene expression profiles (Figure 7). For example, genes activated by HIF-1α but not HIF-2α can also be activated by HIF-2α/1α, but not HIF-1α/2α. Overall, our genomic results show that HIF-α IDR contributes significantly to isoform-specific target site binding and helps determine isoform-specific target gene activation.

Discussion

Transcription factors must search, recognize and bind to their specific target sites among millions of possible DNA sequences along chromatin to activate the correct gene. With the successful development of X-ray crystallography and cryo-EM, mechanisms of DNA-binding specificity have been extensively studied, primarily based on classically structured globular DNA-binding domains of TFs. We now know that a variety of structural mechanisms are used to recognize DNA, including formation of specific hydrogen bonds and DNA contour interactions (Rohs et al., 2010). However, these inherent binding modalities of DBDs alone cannot explain TF binding site selection *in vivo* in eukaryotic cells. As revealed by genome-wide *in vivo* binding assays, only a subset of potential target sites become occupied, and this is not entirely consistent with either DNA binding site affinity or chromatin accessibility (Behera et al., 2018; Grossman et al., 2017; Srivastava and Mahony, 2020). On the other hand, TFs have long been recognized to also contain long unstructured transactivation domains with simple amino acid composition (Gln-rich, acidic, Pro-rich etc.), which often posed challenges to purification and/or crystallization of full-length TFs (Courey and Tjian, 1988; Ma and Ptashne, 1987; Mermod et al., 1989; Tjian and Maniatis, 1994). Recently, such intrinsically disordered regions (IDRs) were reported to play an important role in weak and multivalent protein-protein interactions to form local small transient hubs that, when

408 exacerbated by overexpression, can drive phase separation. Although not structurally defined,
409 these interactions can still be sequence/amino acid composition selective (Chong et al., 2018;
410 Chong and Mir, 2021). IDRs are now proposed to have important functions in boosting gene
411 expression through hub or condensate formation to locally enrich for factors that are needed for
412 transcription (Boijja et al., 2018; Cho et al., 2018; Chong et al., 2018; Sabari et al., 2018; Wei et
413 al., 2020). However, few studies of IDRs have investigated their potential role in DNA binding site
414 search and selection. Some studies reported that for a subset of zinc finger proteins (Sp2 and
415 KLF3), an IDR is critical for *in vivo* binding and specificity (Burdach et al., 2014; Lim et al., 2016;
416 Völkel et al., 2015), and two recent studies using genomic approaches reported the IDR as a
417 determinant for specificity for some of the yeast transcription factors (Brodsky et al., 2020; Gera
418 et al., 2022).
419
420 Here, using advanced live cell single particle tracking, we report that TF IDRs previously
421 associated with ADs are, in fact, a major determinant mediating nuclear search dynamics and
422 chromatin binding characteristics. Employing both genetic and small molecule perturbations
423 together with a series of domain-swap and mutation experiments, we found that it is the AD-
424 associated disordered region of HIF-α rather than the intrinsic molecular weight of the TF that
425 dictates a relatively slow diffusion for both HIF-α monomers and HIF-α/β dimers. On the other
426 hand, when not engaged with HIF-α, HIF-1β diffuses rapidly as expected for an unencumbered
427 subunit. These results indicate that the diffusion characteristic of HIF molecules is profoundly
428 influenced by the properties of their disordered regions (Figure 8A). In fact, computational analysis
429 shows very different amino acid composition bias among HIF-1α, -2α and -1β disordered regions
430 (Figure 1—figure supplement 1B). Thus, it is very likely that as these molecules navigate through
431 the crowded nuclear environment, their distinct stretches of IDRs that also contain ADs make
432 differential and selective interactions with other nuclear components, resulting in distinct diffusive
433 behaviors. According to Coulomb's law, acidity, and thus electrostatic charge on the molecules,
434 contribute to the attraction or repulsion forces towards other molecules in the environment. Thus
435 it is also possible that due to differences in acidity, the different charges on these IDRs can cause
436 differential non-specific interactions with macromolecules including not only proteins, but also
437 DNA and RNA (Xiang et al., 2020).
438
439 While it is easy to conceptualize how IDRs can influence the rate of diffusion, one unexpected
440 result is that they also largely determine how much TFs bind to chromatin, as well as influence
441 their binding site preferences. Although we confirmed that the DBD and dimerization domains are

442 important for chromatin binding, the surprise was that our domain swap experiments clearly
443 demonstrated that the percentage of bound TF is mainly contributed by regions outside of the
444 DBD/dimerization domains. One explanation could be the differential charge propensities of the
445 different disordered regions (Figure 1—figure supplement 1B). For example, the HIF-2α IDR is
446 more positively charged and may not only slow down nuclear exploration but also stabilize
447 chromatin binding, possibly through stronger non-specific interactions with negatively charged
448 chromatin-associated RNA and/or nucleosome-free DNA regions. Besides direct chromatin
449 interactions, HIF-2α IDR could also increase and stabilize binding via indirect interactions with
450 other chromatin-bound proteins. Moreover, since different IDRs can selectively interact with other
451 IDRs (Chong et al., 2018; Chong and Mir, 2021), we also postulate that selective interactions with
452 other TFs or co-regulators may play a role in determining HIF chromatin-binding specificity. One
453 hint of such a "combinatorial TF selectivity mechanism" is the enrichment of different transcription
454 factor motifs at HIF-1α and HIF-2α binding sites. Depending on the cell type, AP-1 or FOXD2,
455 FOXL1 and FOXC2 were previously found at HIF-2α binding sites, while HEY1/2, ZNF263 or
456 SP1/2 were found at HIF-1α binding sites (Smythies et al., 2019). It was also previously reported
457 that while no target specificity was preserved in reporter gene assays, the N-terminal TAD of HIF-
458 α conferred endogenous target specificity for two of the HIF-1 unique genes examined, possibly
459 via specific interactions with transcriptional cofactors (Hu et al., 2007). Further Co-IP or pull-down
460 assay coupled with mass spectrometry (MS) will be needed to more fully dissect this type of *in*
461 *vivo* selectivity mechanism.
462
463 Given our results, we believe that the simple "division of labor" model for DBDs and IDRs is an
464 over-simplification which was probably only suitable for prokaryotes. Instead, eukaryotic TFs have
465 evolved to exploit both DBDs and IDRs for chromatin binding as well as binding site selection,
466 which is best suited for the eukaryotic chromatin environment. We propose that TF-chromatin
467 engagement (binding and site selection) comprises two components – the first being DBD-
468 mediated, mainly the classical motif binding force that acts directly on DNA, and the second being
469 IDR-mediated interactions (likely weak and multivalent) with the native chromatin environment
470 that include protein-protein interactions, and interactions with DNA and RNA molecules. Thus, we
471 want to emphasize that the term "DNA binding specificity" refers to the first interaction component
472 and we propose it should only be used with respect to isolated or naked DNA in eukaryotes.
473 Instead, "chromatin binding preferences" would be a better term to describe *in vivo* binding
474 preferences of eukaryotic TFs within a native chromatin environment, which not only include DBD-
475 DNA interactions, but also involve "micro-environment recognition" mediated by IDR-chromatin

476 interactions. These two forces can be additive or competitive, depending on the macromolecule
477 composition of each specific chromatin locus, resulting in varied TF occupancy that could not be
478 simply predicted from the DNA code. It seems that in the case of HIFs, for most of their binding
479 sites the combined DBD- and IDR-mediated forces are similar for both HIF-1α and -2α, resulting
480 in overlapping occupancy for different isoforms at these sites. However, for a few but striking
481 cases, IDR-mediated interaction dominates HIFs' binding preferences, modulating the amount of
482 HIF isoforms at these differentially regulated sites (Figure 8B). Interestingly, Myc, a closely related
483 bHLH-LZ family transcription factor, shows predominately DBD-mediated chromatin engagement,
484 where non-specific DBD-DNA interactions contribute most of the binding (Pellanda et al., 2021).
485 These different observations suggest that different eukaryotic transcription factors may exploit
486 DBD- and IDR-mediated interactions to different degrees, resulting in distinct chromatin
487 engagement mechanisms.
488
489 We note that IDR-mediated chromatin engagement could happen either before and after DNA
490 binding. It is possible that these IDR-mediated interactions first locate the TF to a few highly
491 concentrated protein hubs in the vicinity of selected genomic binding sites, and then the TF
492 performs a more localized target search with the DBD to find its motif, as it has been recently
493 proposed (Jana et al., 2021; Darzacq and Tjian, 2022; Staller, 2022). In this case, whether the TF
494 explores the nucleus alone to join the hubs or explores it as a larger complex containing other
495 TFs/coactivators, IDRs both determine the TF dynamics and significantly improves the TF on-
496 rate. On the other hand, it is also possible that TFs first binds to their target site via the DBD, and
497 then IDR-mediated interactions stabilize the binding, increasing the TF's residence time and
498 decreasing its off-rate. In both cases, distinct IDRs among different TF from closely related family
499 members can create isoform-specific binding (and thus achieve isoform-specific gene activation)
500 at selected genomic sites amongst all binding sites that are shared by the same family.
501
502 Finally, we have demonstrated that our fSPT platform provides a powerful tool able to resolve *in*
503 *vivo* protein dynamics that is exquisitely sensitive to concentration, subunit stoichiometry and
504 genetic/small molecule perturbations. This is especially important when studying TFs, where a
505 slight difference in expression level often generates completely different results, rendering over-
506 expression systems highly susceptible to artifacts. It is also worth underscoring the importance of
507 studying TFs in their native physiologically relevant chromatin environment, given their obligate
508 interactions with higher-order chromatin structures and cofactors. For example, the EPO gene is
509 reported to be responsive to HIF-2α but not HIF-1α in Hep3B cells (Warnecke et al., 2004) and in

510 murine liver (Rankin et al., 2007), however, a luciferase reporter driven by the upstream EPO
511 enhancer also responds strongly to HIF-1α (Varma and Cohen, 1997), which may generate
512 misleading results and interpretations. Our fSPT platform allows us to study transcriptional
513 regulation in the native chromatin context and with endogenous TF levels to obtain data with
514 physiological and functional relevance. Such live cell real time measurements under native cell
515 contexts could prove to be highly valuable, both for dissecting *in vivo* mechanisms of transcription
516 regulation, and for guiding the development of effective therapeutics. Our Belzutifan treatment
517 experiment is an example of how fSPT can reveal the mechanism of action of small molecule
518 inhibitors, and how it could serve as a powerful tool to screen for drugs that selectively target one
519 isoform versus another, using dimerization and binding readouts as indicators of efficacy and
520 specificity. Moreover, since our results demonstrated how IDRs can affect TF diffusion behavior,
521 potentially distinct dynamic features determined by a particular IDR can be exploited as a readout
522 for screening small molecules or peptides that target allosteric sites of TFs. Assays that can
523 quantitatively measure TF diffusive behavior in live cells could be transformative for advancing
524 drug discovery because a high throughput imaging strategy opens the door to effectively target
525 what has been traditionally considered "undruggable", such as most protein-protein interactions
526 including potentially unstructured TF activation domains.
527
528 In summary, using the HIF protein family as a case study, we uncovered a mechanism of IDR-
529 mediated nuclear search and differential chromatin binding leading to selective gene activation.
530 We expect this fundamental principle to be applicable to a broad range of TF families.
531
532 **Materials and Methods**
533
534 **Cell culture, stable cell line construction and drug treatment**
535 Human 786-O clear cell renal carcinoma cells were obtained from the UCB Cell Culture Facility
536 (RRID:SCR_017924), which were originally obtained from ATCC (#CRL-1932). The cells were
537 tested for mycoplasma using nuclear stain with a 100X lens on a fluorescence scope on 1/22/2020
538 when banked and STR was used to identify them on 1/24/2020. Cells were cultured at 37°C with
539 5% CO2 in 4.5 g/L glucose DMEM (ThermoFisher, Waltham, MA, #10566016) supplemented with
540 10% Fetal Bovine Serum (HyClone, Logan, UT, Cat. #SH30396.03, lot #AE28209315), 1 mM
541 Sodium Pyruvate (ThermoFisher #11360070) and 100 U/mL Penicillin-Streptomycin
542 (ThermoFisher #15140122). Cells were subcultured at a ratio of 1:4 to 1:12 every 2 to 4 days for
543 no longer than 30 days. A regular mycoplasma testing was performed every two weeks using

544 PCR. Phenol red-free DMEM (ThermoFisher, #21063029) supplemented with 10% Fetal Bovine
545 Serum, 1 mM Sodium Pyruvate and 100 U/mL Penicillin-Streptomycin was used for imaging.
546
547 Stable cell lines expressing the exogenous gene product (Table 4) were generated by PiggyBac
548 transposition and antibiotic selection. The gene of interest was cloned into a PiggyBac vector
549 which also co-expresses a puromycin resistant gene using Gibson Assembly and confirmed by
550 Sanger sequencing. Cells were transfected by nucleofection using the Lonza Cell Line
551 Nucleofector® Kit V (Lonza, Basel, Switzerland, #VVCA-1003) and the Amaxa Nucleofector II
552 device. For each transfection, cells were plated 1-2 days before nucleofection in a 15-cm dish,
553 and reached approximately 50-70% confluency on the day of nucleofection, which equals to
554 approximately 3-4 million cells. 2 µg of PiggyBac plasmid was co-transfected with 1 µg of
555 SuperPiggyBac transposase vector with the T-020 program according to manufacturer's protocol.
556 Transfected cells were cultured for 24-48 hours before changing to selection media. Cells were
557 then selected for 14 days with 1 µg/ml puromycin (ThermoFisher #A1113803) and stable cell lines
558 were maintained in selection media for up to 30 days of culturing.
559
560 For drug treatment, 100 mM Belzutifan stock solution was prepared by dissolving Belzutifan
561 powder (CAS No: 1672668-24-4, MedChemExpress, Monmouth Junction, NJ, Cat. #HY-125840)
562 in DMSO (Sigma, St. Louis, MO, #D2650), and was diluted 1:500,000 in growth media to the final
563 concentration of 0.2 µM. The same volume of DMSO (0.0002%) is used in the reference group
564 as control. Cells were treated for 24 hours in either Belzutifan or DMSO alone before imaging.
565 For dosage-dependent assays in Figure 3—figure supplement 1, DMSO amount was kept the
566 same (0.0002%) for all drug concentrations.
567
568 **CRISPR/Cas9-mediated genome editing**
569 Knock-in cell lines were generated as previously described (Hansen et al., 2017) with the following
570 changes. For each editing case, we designed 3 sgRNAs using CRISPOR (Concordet and
571 Haeussler, 2018). For each guide/donor pair, approximately 4 million 786-O cells were
572 nucleofected with 3.75 µg of donor plasmid and 1.25 µg of sgRNA plasmid. 24 hours after
573 transfection, Venus-positive cells were sorted and cultured for another 5-7 days, then Halo-
574 positive cells were sorted individually into single wells of 96 well plates. Clones were expanded
575 and genotyped with two rounds of PCR. The first round used one primer upstream of the left
576 homologous arm and the other primer downstream of the right homologous arm. The second
577 round used either of the external primers and a corresponding internal primer located in the

578 HaloTag coding region. Homozygous clones with the correct genotype, including Halo-HIF-2α
579 KIN clone A31 and clone B50, Halo-HIF-1β KIN clone A21 and clone B89, were confirmed by
580 Sanger sequencing and western blotting.
581
582 **Cell preparation and dye labeling for imaging**
583 For fast SPT, cells were grown on sonicated and plasma-cleaned 25-mm circular no 1.5H
584 precision cover glass (Marienfeld, Germany, 0117650) in 6-well plate. At least one day before
585 imaging, selective medium (if used) was removed and replaced with non-selective growth medium.
586 On the day of imaging, cells should be less than 100% confluent. Immediately before imaging,
587 cells were double labeled with JFX dyes as follows: cells were first incubated for 5 min in 1 ml
588 growth medium containing JFX 646, at a concentration that only gives approximately 10 detected
589 molecules per frame in the initial frames to ensure minimum misconnection of trajectories
590 between detections. This concentration differs from cell line to cell line, ranging from 0.2 – 5 nM,
591 depending on the expression level of the Halo-fusion protein. After 5 min of incubation, medium
592 was removed, cells were rinsed in PBS, and incubated for 5 min in 1 ml medium containing JFX
593 549. The concentration of JFX 549 also varies, usually at 25x the concentration of JFX 646. After
594 incubation, cells were washed twice for 5 min each, a first time with 2 ml regular growth media,
595 and a second time with 2 ml phenol red-free growth media, with a quick PBS rinse before each
596 wash. After wash, coverslip was transferred to Attofluor Cell Chambers (ThermoFisher, #A7816)
597 with cells facing up and 1 ml phenol red-free medium added to the chamber. For Belzutifan
598 treatment experiments, Belzutifan or equivalent amount of DMSO was added throughout the
599 labeling and washing steps (except during PBS rinses), as well as in the final imaging medium,
600 at the indicated concentration.
601
602 **Live Cell Single particle tracking**
603 All SPT experiments were carried out on a custom-built microscope as previously described
604 (Hansen et al., 2017) (McSwiggen et al., 2019). In brief, a Nikon TI microscope is equipped with
605 a 100x/ NA 1.49 oil-immersion TIRF objective, a motorized mirror, a perfect Focus system, an
606 EM-CCD camera and an incubation chamber maintained with humidified atmosphere with 5%
607 CO2 at 37 °C. All microscope, camera and hardware components were controlled through the
608 NIS-Elements software (Nikon).
609
610 During imaging, samples were excited with 561-nm laser at 1100 mW (Genesis Coherent, Santa
611 Clara, CA) with emission filter set to Semrock 593/40 nm band-pass filter to locate and focus the

612 cell nuclei, as well as to adjust laser angle to achieve highly inclined laminated optical sheet (HiLo)
613 illumination (Tokunaga et al., 2008). An ROI (Regions of Interest) of random size was selected to
614 fit into the interior of the nuclei but with maximized area. Then the emission filter was switched to
615 Semrock 676/37 nm bandpass filter while keeping TIRF angle, stage xyz position and ROI the
616 same. Movies were then taken with 633-nm laser (Genesis Coherent, Santa Clara, CA) at 1100
617 mW and 1 ms pulse, with camera exposure at 5.48-ms frame rate for 800-1600 frames, until
618 samples were completely photo-bleached. At least 20 movies (corresponding to 20 cells) were
619 taken for each sample as one biological replicate on a given day. A total of three biological
620 replicates on three separate days were collected to produce the final results (>60 cells per cell
621 line/condition).
622
623 **SPT data processing**
624 Raw SPT movies were processed with a publicly available single particle tracking package
625 (https://github.com/alecheckert/quot) to generate trajectory files (.trajs). Generally, it performs
626 tracking in the following steps: read a frame, find spots in the frame, localize spots to subpixel
627 resolution, and reconnect spots from consecutive frames into trajectories. Since a non-
628 photoactivatable dye was used for all SPT experiments, we labeled cells with a dye concentration
629 that only gives very low spot detection density, which allowed us to track spots since the first
630 frame. This is important because if the initial frames are filtered due to high localization density,
631 there might be a bias towards moving molecules, due to the bound molecules being
632 photobleached and diffusing molecules moving into the focal plane during the later frames.
633 Although we used very sparse labeling, occasionally there would be frames with high density, to
634 minimize misconnections due to multiple particles in close proximity, we incorporated a filtering
635 step where we removed frames with more than 7 detections in the following way. First, we
636 computed the number of detections per frame. Next, this function was smoothed with uniform
637 filtering with a kernel width of 21 frames. Finally, we identified frames with fewer than 7 detections
638 after smoothing and isolated trajectories from these frames. Specifically, the following
639 configuration was used for all detections and tracking: Image reading and filtering settings: start
640 = 0, method = “identity”, chunk_size = 100; Spot detection settings: method = “llr”, k = 1.0, w = 15,
641 t = 18; Subpixel localization settings: method = 'ls_int_gaussian', window_size = 9, sigma = 1.0,
642 ridge = 0.001, max_iter = 20, damp = 0.3; Tracking settings: method = 'euclidean',
643 max_spots_per_frame = 7, pixel_size_um = 0.16, frame_interval = 0.00548, search_radius = 1.0,
644 max_blinks = 0, min_I0 = 0.0, scale = 7.0.
645

646 To infer the distribution of diffusion coefficients from experimentally observed trajectories, we
647 used a publicly available implementation of state arrays (https://github.com/alecheckert/spagl)
648 (`sample_script_fss.py`), which generates the posterior mean occupations for a state array
649 evaluated on trajectories across all cells. In all analyses, we used the likelihood function for
650 regular Brownian with localization error (RBME) (Heckert et al., 2021). Settings were:
651 frame_interval = 0.00548, pixel_size_um = 0.16, dz = 0.7. Occupations are reported as the
652 mean of the posterior distribution over state occupations, marginalized on diffusion coefficient.
653
654 To generate RBME likelihood for individual cells, we used the `sample_script_by_file.py`
655 script in the same repository (https://github.com/alecheckert/spagl) (Heckert et al., 2021) with
656 the following settings: frame_interval = 0.00548, dz = 0.7, pixel_size_um=0.16,
657 scale_by_total_track_count = True, scale_colors_by_group = True.
658
659 **Antibodies**
660 The following antibodies were used for ChIP-seq: rabbit polyclonal anti-HIF-2α (Novus Biologicals,
661 Centennial, CO, #NB100-122), mouse monoclonal anti-HIF-1β (Novus Biologicals, #NB100-124),
662 rabbit polyclonal anti-V5 (Abcam, Cambridge, UK, #ab9116). The following antibodies were used
663 for Cut&Run: mouse monoclonal anti-V5 tag (ThermoFisher, # R960-25) diluted to 0.01 mg/ml,
664 mouse IgG (Jackson ImmunoResearch #015-000-003) diluted to 0.01 mg/ml, rabbit anti-mouse
665 IgG H&L (Abcam, #ab46540) diluted to 0.01 mg/ml. The following antibodies were used for
666 western blotting: rabbit monoclonal anti-HIF-2α (Cell Signaling, Danvers, MA, #D9E3) diluted at
667 1:1000, rabbit monoclonal anti-HIF-1β (Cell Signaling, #D28F3) diluted at 1:1000, mouse
668 monoclonal anti-V5 tag (ThermoFisher, # R960-25) diluted at 1:2500, mouse monoclonal anti-
669 HaloTag (Promega, Madison, WI, # G9211) diluted at 1:1000, mouse monoclonal anti-TBP
670 (Abcam, #ab51841) diluted at 1:2500, goat-anti-mouse-HRP (ThermoFisher, #31430) diluted at
671 1:2000, goat-anti-rabbit-HRP (ThermoFisher, # 31462) diluted at 1:2000.
672
673 **Western blotting**
674 All western samples were prepared as follows: cells growing in either 6-well plates or 10-cm dish
675 in log phase were rinsed with PBS twice and lysed on ice in 100-500 ul 2x Sample buffer (80 mM
676 Tris pH6.8, 2% SDS, 10% Glycerol, 0.0006% Bromophenol blue) containing 280 mM 2-
677 Mercaptoethanol (Sigma #M7522), 1x Aprotinin (Sigma, #A6279, diluted 1:1000), 1 mM
678 Benzamidine (Sigma, #B6506), 1x cOmplete™ EDTA-free Protease Inhibitor Cocktail (Sigma,
679 #5056489001), and 0.25 mM PMSF (Sigma #11359061001). Cell lysates were scraped and

680 collected into 1.5-ml Eppendorf tubes, incubated at 99 °C with constant shaking, snap frozen in
681 liquid nitrogen and stored at -80 °C. On the day of western blotting, samples were thawed and
682 centrifuged at top speed for 5 min at 4 °C. Ten to 15 µl supernatant were loaded on an 8% SDS-
683 Page gel, ran for 1h at 200 V and 4 °C, and transferred to 0.45-µm nitrocellulose membrane
684 (Fisher, # 45004031) for 2 hrs at 100V. Membranes were blocked in 10% milk in 0.1% TBS-Tween
685 for 1 hr at RT, and incubated overnight at 4 °C with primary antibodies diluted in 5% milk in 0.1%
686 TBS-Tween. After 4 x 5 min washes in 0.1% TBS-Tween, membranes were incubated at RT for
687 at least 1 h with secondary antibodies diluted in 5% milk in 0.1% TBS-Tween. After 4 x 5 min
688 washes in 0.1% TBS-Tween, membranes were incubated for 3 min in freshly made Perkin Elmer
689 LLC Western Lightning Plus-ECL, Enhanced Chemiluminescence Substrate (Fisher,
690 #509049326), and imaged with a Bio-Rad ChemiDoc imaging system (BioRad, Model No:
691 Universal Hood III). For reblotting, membranes were immersed in Restore™ Western Blot
692 Stripping Buffer (Fisher, #21059) for 15 min at RT with shaking, washed 3 x 10 min in 0.1% TBS-
693 Tween, followed by blocking, antibody incubation and chemiluminescence reaction as described
694 above.
695
696 **Luciferase reporter assay**
697 The firefly luciferase reporter gene construct was made by inserting a 3x Hypoxia Responsive
698 Elements (HREs) from the EPO gene enhancer (sequence:
699 tcgaagccctacgtgctgtctcacacagcctgtctgacctctcgacctaccggccgttcgaagccctacgtgctgtctcacacagccttct
700 gatctcgacctaccggccgttcgaagccctacgtgctgtctcacacagcctgtctgacctctcgacctaccggccgt) into the 5' of
701 the minimal TATA-box promoter in the pGL4.23 [luc2/minP] vector (Promega #E841A). A control
702 pHRL-TK vector (Promega #E2241) expressing Renilla luciferase with an HSV TK promoter was
703 used as reference to normalize luciferase activity. Cells were co-transfected with 1 ug of firefly
704 Luciferase vector and 0.1 ug Renilla luciferase vector by nucleofection with Lonza Cell Line
705 Nucleofector® Kit V (Lonza, #VVCA-1003) and the T-020 program in the Amaxa Nucleofector II
706 device. After nucleofection, cells were resuspended in complete growth medium, and plated into
707 12-well plates with Belzutifan added to various concentrations as indicated. 24 hours after
708 nucleofection, cells were lysed and luciferase activity was analyzed with Dual-luciferase Reporter
709 Assay System (Promega, #E1960) according to manufacturer's protocol. The relative luciferase
710 activity was calculated by normalizing firefly luciferase activity to the Renilla luciferase activity to
711 control for transfection efficiency.
712
713 **Chromatin Immunoprecipitation and ChIP-seq library preparation**

714 ChIP was performed as described with few modifications (Testa et al., 2005). Wild type 786-O or
715 endogenously tagged knock-in clones A31 (V5-Halo-HIF-2α) and A21 (V5-Halo-HIF-1β) were
716 expanded to two 15-cm dishes and cross-linked 5' at room temperature with 1% formaldehyde-
717 containing FBS-free medium; cross-linking was stopped by adding PBS-glycine (0.125 M final).
718 Cells were washed twice with ice-cold PBS, scraped, centrifuged for 10' and pellets were flash-
719 frozen. Cell pellets were thawed and resuspended in 2 ml of cell lysis buffer (5 mM PIPES, pH
720 8.0, 85 mM KCl, and 0.5% NP-40, 1 ml/15 cm plate) w/ protease inhibitors and incubated for 10'
721 on ice. Lysates were centrifuged for 10' at 4000 rpm and nuclear pellets resuspended in 6 volumes
722 of sonication buffer (50 mM Tris-HCl, pH 8.1, 10 mM EDTA, 0.1% SDS) w/ protease inhibitors,
723 incubated on ice for 10', and sonicated to obtain DNA fragments around 500 bp in length (Covaris
724 S220 sonicator, 20% Duty factor, 200 cycles/burst, 150 peak incident power, 10 cycles 30" on
725 and 30" off). Sonicated lysates were cleared by centrifugation and chromatin (400 μg per antibody)
726 was diluted in RIPA buffer (10 mM Tris-HCl, pH 8.0, 1 mM EDTA, 0.5 mM EGTA, 1% Triton X-
727 100, 0.1% SDS, 0.1% Na-deoxycholate, 140 mM NaCl) w/ protease inhibitors to a final
728 concentration of 0.8 μg/μl, precleared with Protein G sepharose (GE Healthcare) for 2 hours at
729 4°C and immunoprecipitated overnight with 4 μg of specific antibodies. About 4% of the
730 precleared chromatin was saved as input. Immunoprecipitated DNA was purified with the Qiagen
731 QIAquick PCR Purification Kit, eluted in 33 μl of 0.1X TE (1 mM Tris-HCl pH 8.0, 0.01 mM EDTA)
732 and analyzed by qPCR together with 2% of the input chromatin prior to ChIP-seq library
733 preparation (SYBR® Select Master Mix for CFX, ThermoFisher). ChIP-qPCR primer sequences
734 were as follows:
735 hWISP1_positive_forward: TGAGGTCAGTGTGGTTTGGT
736 hWISP1_positive_reverse: ACATGGTCACGTAGCTAGCA
737 hWISP1_negative_forward: AGTCCCCAGCACATAGAAGG
738 hWISP1_negative_reverse: GGTTCTGAAGGTGACCGACT
739 ChIP-seq libraries were prepared using the NEBNext® Ultra™ II DNA Library Prep Kit for Illumina®
740 (NEB E7645) according to manufacturer instructions with a few modifications. 20 ng of ChIP input
741 DNA (as measured by Nanodrop) and 25 μl of the immunoprecipitated DNA were used as a
742 starting material and the recommended reagents' volumes were cut in half. The NEBNext Adaptor
743 for Illumina was diluted 1:10 in Tris/NaCl, pH 8.0 (10 mM Tris-HCl pH 8.0, 10 mM NaCl) and the
744 ligation step extended to 30'. After ligation, a single purification step with 0.9X volumes of
745 Agencourt AMPure XP PCR purification beads (Beckman Coulter A63880) was performed, eluting
746 DNA in 22 μl of 10 mM Tris-HCl pH 8.0. 20 μl of the eluted DNA were used for the library
747 enrichment step, performed with the KAPA HotStart PCR kit (Roche Diagnostics KK2502) in 50

748 μl of total reaction volume (10 μl 5X KAPA buffer, 1.5 μl 10 mM dNTPs, 0.5 μl 10 μM NEB
749 Universal PCR primer, 0.5 μl 10 μM NEB index primer, 1 μl KAPA polymerase, 16.5 μl nuclease-
750 free water and 20 μl sample). Samples were enriched with 9 PCR cycles (98 °C, 45"; [98 °C, 15";
751 60 °C, 10"] x 9; 72 °C, 1'; 4 °C, hold), purified with 0.9 volumes of AMPure XP PCR purification
752 beads and eluted with 33 μl of 10 mM Tris-HCl pH 8.0. Library concentration, quality and fragment
753 size were assessed by Qubit fluorometric quantification (Qubit™ dsDNA HS Assay Kit,
754 Invitrogen™ Q32851) qPCR and Fragment analyzer™. 12 multiplexed libraries (input, HIF1-β,
755 HIF1-α and V5 pulldowns in WT 786O cells and A31 and A21 clones) were pooled and sequenced
756 in one lane on the Illumina HiSeq4000 sequencing platform (50-bp, single end-reads) at the
757 Vincent J. Coates Genomics Sequencing Laboratory at UC Berkeley.
758
759 **ChIP-seq analysis**
760 ChIP-seq raw reads from WT 786O cells and A31 and A21 endogenously Halo-tagged clones (12
761 libraries total, 1 replicate per condition) were quality-checked with FastQC 0.10.1 and aligned
762 onto the human genome (hg38 assembly) using Bowtie (Langmead et al., 2009), allowing for two
763 mismatches (-n 2) and no multiple alignments (-m 1). Peaks were called with MACS2
764 2.1.0.20140616 (--nomodel --extsize 300) (Zhang et al., 2008) using input DNA as a control. To
765 create heatmaps we used deepTools 2.4.1 (Ramírez et al., 2016). We first ran bamCoverage (--
766 binSize 50 --normalizeTo1x 2913022398 --extendReads 300 --ignoreDuplicates -of bigwig) and
767 normalized read numbers to 1x sequencing depth, obtaining read coverage per 50-bp bins across
768 the whole genome (bigWig files). We then used the bigWig files to compute read numbers across
769 6 kb centered on HIF-2α peaks called by MACS2 across all 786O cell lines, subtracted of V5
770 peaks called by MACS2 in WT 786O cells (computeMatrix reference-point --referencePoint=TSS
771 --upstream 3000 --downstream 3000 --missingDataAsZero --sortRegions=no). We sorted the
772 output matrices by decreasing WT 786O enrichment, calculated as the total number of reads
773 within a MACS2 called ChIP-seq peak. Finally, heatmaps were created with the plotHeatmap tool
774 (--averageTypeSummaryPlot=mean --colorMap='Blues' --sortRegions=no).
775
776 **Cut&Run**
777 Cut&Run was performed as published (Janssens and Henikoff, 2019) with the following
778 modifications / specifications. Around 0.5 million cells were used for each experimental condition.
779 Before permeabilization, proteinase inhibitor was left out from the buffer to minimize toxicity to the
780 cells, but was added during the permeabilization step. Digitonin was used at a final concentration

781 of 0.02% for Dig wash buffer and antibody buffer, as it was tested to be the minimum concentration
782 to fully permeabilize 786-O cells. For each cell line, a primary antibody (either mouse-anti-V5 or
783 mouse IgG, 1mg/ml at 1:100 dilution) was used with a 4 ºC overnight incubation. A secondary
784 rabbit-anti-mouse IgG was used at 1:100 dilution with an hour incubation at 4 ºC. For each wash,
785 100 µl of Dig-wash buffer was used. Chromatin digestion was done for 30 minutes on ice. DNA
786 was extracted with phenol / chloroform and the pellet was dissolved in 30 µl 0.1 x TE (1 mM Tris-
787 HCl pH 8 0.1 mM EDTA). DNA was quantified by Qubit (Qubit™ dsDNA HS Assay Kit,
788 InvitrogenTM Q32851) and up to 40 ng (and up to 25 µl) was used for library preparation, using
789 NEBNext® Ultra™ II DNA Library Prep Kit for Illumina® (NEB E7645) according to manufacturer
790 instructions, with a few modifications. Reagents' volumes were cut in half. For end prep 20 ºC 30
791 min followed by 50 ºC 60 min was used. For adapter ligation, NEBNext Adapter was diluted 1:20
792 in Tris/NaCl, pH 8.0 (10 mM Tris, 10 mM NaCl), mixture was incubated for 30 min at 20 ºC (instead
793 of 15 min). After ligation, product was size-selected with 1.75x Agencourt AMPure XP PCR
794 purification beads (Beckman Coulter A63880), and DNA was eluted in 15 µl 10 mM Tris-HCl pH
795 8.0. 13 ul of eluted DNA was used for library enrichment with 15 µl NEBNext Ultra II Q5 Master
796 mix, 1 µl 10 µM NEB Universal PCR primer and 1 µl 10 µM NEB Index Primer. Samples were
797 enriched with 11 PCR cycles (98 °C, 30"; [98 °C, 10"; 65 °C, 10"] x 11; 65 °C, 5'; 4 °C, hold). The
798 30 µl PCR product was size-selected with double AMPure XP cleanup (first with 24 µl (0.8x) beads
799 and take the supernatant, then add 12 µl beads (to final PEG/NaCl 1.2x) and discard supernatant).
800 Library was eluted with 15 µl 10 mM Tris-HCl pH 8.0 and quantified by Qubit (Qubit™ dsDNA HS
801 Assay Kit, InvitrogenTM Q32851). Libraries were sent to MedGenome Inc. (Foster City, CA, USA)
802 for fragment analysis, multiplexing and sequencing on the Illumina NovaSeq 6000 platform (150
803 bp, paired end reads).
804
805 **Cut&Run data analysis**
806 Cut&Run raw fastq reads were first quality-checked with FastQC
807 (http://www.bioinformatics.babraham.ac.uk/projects/fastqc) and then aligned to the human
808 genome (hg38) using bowtie2 version 2.3.4.1 with options: --local --no-unal --very-sensitive --no-
809 mixed --no-discordant --phred33 -I 10 -X 700. Non-human chromosomes were removed, then
810 bam files were created using Samtools (Li et al., 2009) version 1.8. Then Sambamba (Tarasov et
811 al., 2015) version 0.6.6 was used to sort bam files, and filter unmapped reads. Finally, samtools
812 were used to index the files. For peak calling with MACS2 (--keep-dup all --max-gap 400 -g hs --
813 bdg -q 0.01 -f BAMPE) (Zhang et al., 2008), mouse IgG control was used as control for each cell
814 line. Blacklisted regions were removed from the output narrowpeak file with BEDTools (Quinlan

815 and Hall, 2010) version 2.28.0. For visualization of genome-wide binding strength on the hg38
816 genome with the Integrative Genomics Viewer (IGV) (Robinson et al., 2011; Thorvaldsdóttir et al.,
817 2013), individual replicates were first combined into a single bam file using Samtools version 1.8,
818 and then converted to bigWig output files from deepTools bamCoverage (--binSize 20 --
819 normalizeUsing BPM --smoothLength 60). The PCA and clustering analysis, as well as
820 identification of differentially bound regions by HIF-1α and HIF-2α were done with DiffBind (Stark
821 and Brown, 2011) version 3.0, with all three replicates as samples. The final HIF-1α and HIF-2α
822 responsive regions were obtained by filtering the list with P value <0.01. Heatmaps for binding
823 strength were generated for each individual replicate or the combined replicates, using deepTools
824 (Ramírez et al., 2016) version 3.5.1.
825
826 **RNA extraction and poly-A RNA-Seq library preparation**
827 Poly-A RNA-Seq was performed in two batches and three biological replicates per sample. In the
828 first batch (3 replicates each of WT 786-O cells, HIF-1b KI, HIF-2a KI, HIF-1a O.E., HIF-1a R30E,
829 HIF-1a DM, HIF-2a O.E., HIF-2a R27E, HIF-2a DM) total RNA was extracted with the QIAGEN
830 RNeasy Plus Mini Kit (74134) according to manufacturer instructions, quantified by NanoDrop
831 and checked for integrity by capillary electrophoresis. 1 µg of the purified RNA was added of
832 ERCC RNA Spike-In Mix 2 (ThermoFisher Scientific #4456740, 0.5-1 µl of a 1:100 dilution per
833 sample) and the total volume brought to 50 µl with UltraPure Water (ThermoFisher Scientific #
834 10977-023). mRNA purification, RNA fragmentation, first and second strand cDNA synthesis were
835 performed according to the TruSeq RNA Sample Preparation v2 Kit (Illumina RS-122-2001) using
836 Superscript III for reverse transcription instead of Superscript II (incubation time: 50 °C for 50 min).
837 cDNA was purified with AMPure XP beads and eluted in 27.5 µl 10 mM Tris-HCl pH 8.0, 25 µl of
838 which were transferred to a new tube and subjected to a NEBNext® Ultra™ II DNA Library Prep
839 Kit for Illumina (NEB #E7645), using half of the recommended reagents' volumes. The NEBNext
840 Adaptor for Illumina was diluted 1:5 in Tris/NaCl, pH 8.0 (10 mM Tris-HCl pH 8.0, 10 mM NaCl)
841 and the ligation step extended to 30'. Library enrichment was performed with the KAPA HotStart
842 PCR kit (Roche Diagnostics KK2502) in 50 µl of total reaction volume (10 µl 5X KAPA buffer, 1.5
843 µl 10 mM dNTPs, 0.5 µl 10 µM NEB Universal PCR primer, 0.5 µl 10 µM NEB index primer, 1 µl
844 KAPA polymerase, 16.5 µl nuclease-free water and 20 µl sample). Samples were enriched with
845 8 PCR cycles (98 °C, 45"; [98 °C, 15"; 60 °C, 10"] x 9; 72 °C, 1'; 4 °C, hold), purified with 0.9
846 volumes of AMPure XP PCR purification beads and eluted with 33 µl of 10 mM Tris-HCl pH 8.0.
847 Library concentration, quality and fragment size were assessed by Qubit fluorometric
848 quantification (Qubit™ dsDNA HS Assay Kit, InvitrogenTM Q32851) qPCR and Fragment

849 analyzer™. Multiplexed libraries were pooled and sequenced on the Illumina NovaSeq 6000
850 platform (50-100 bp, paired-end reads) at the Vincent J. Coates Genomics Sequencing
851 Laboratory at UC Berkeley, supported by NIH S10 OD018174 Instrumentation Grant.
852
853 In the second batch (3 replicates each of WT 786-O cells, HIF-1a O.E., HIF-2a/1a, HIF-2a O.E.,
854 HIF-1a/2a) total RNA was extracted with TRIzol™ (Thermo Fisher Scientific #15596026)
855 according to manufacturer instructions, performing an additional wash with 1 volume of chloroform
856 after the recommended phenol:chloroform extraction. RNA was quantified by NanoDrop and
857 checked for integrity by capillary electrophoresis. 5 µg of total RNA were DNase treated (Ambio
858 #AM1906) and 1 µg of DNase-free RNA was subject to poly-A purification and library preparation
859 with the NEBNext Poly(A) mRNA Magnetic Isolation Module (NEB #E7490S) in combination with
860 the NEBNext Ultra II RNA Library Prep Kit for Illumina (NEB #E7770S). The NEBNext Adaptor for
861 Illumina was diluted 1:5 in Tris/NaCl, pH 8.0 (10 mM Tris-HCl pH 8.0, 10 mM NaCl) and the ligation
862 step extended to 30'. Libraries were enriched with 8 PCR cycles. Library concentration was
863 assessed by Qubit quantification (Qubit™ dsDNA HS Assay Kit, InvitrogenTM Q32851).
864 Multiplexed libraries were pooled and sequenced on the Illumina NovaSeq 6000 platform (150 bp,
865 paired end reads) by MedGenome Inc. (Foster City, CA, USA).
866
867 **RNA-Seq analysis**
868 RNA-Seq raw reads were quality-checked with FastQC
869 (http://www.bioinformatics.babraham.ac.uk/projects/fastqc) and aligned onto the human genome
870 (hg38) using STAR 2.6.1d RNA-Seq aligner (Dobin et al., 2012) with the following options: --
871 outSJfilterReads Unique --outFilterMultimapNmax 1 --outFilterIntronMotifs RemoveNoncanonical
872 --outSAMstrandField intronMotif. We used Samtools 1.9 (Li et al., 2009) to convert STAR
873 output .sam files into .bam files, and to sort and index them. We then counted how many reads
874 overlapped an annotated gene (GENECODE v32 annotations) using HTSeq 0.11.0 (Anders et al.,
875 2014) (htseq-count --stranded=no -f bam --additional-attr=gene_name -m union), and used the
876 output counts files to find differentially expressed genes with DESeq2 (Love et al., 2014), run with
877 default parameters within the Galaxy platform (Blankenberg et al., 2010; Giardine et al., 2005;
878 Goecks et al., 2010). Differentially expressed genes (DEG) were called using and adjusted P-
879 value ≤ 0.01, a fold change ≥ 2 and ≥ 0.5 mean counts. Gene transcript levels were visualized on
880 the hg38 genome with the Integrative Genomics Viewer (IGV) (Robinson et al., 2011;
881 Thorvaldsdóttir et al., 2013) using the bigWig output files from deepTools bamCoverage (--binSize
882 50 --extendReads 250 –normalizeUsingRPKM).

883

884 **Datasets and accession numbers**

885 All high throughput sequencing data generated in this publication have been deposited in NCBI's
886 Gene Expression Omnibus (Edgar et al., 2002) and are accessible through GEO Series accession
887 number GSE207575. SPT raw data are accessible through DOI: 10.5281/zenodo.5559234.

888

889 **Acknowledgments**

890 We thank Luke Lavis for providing fluorescent HaloTag ligands; the CRL Flow Cytometry Facility
891 for assistance with cell sorting; the QB3 High Throughput Screening Facility for providing access
892 to the Opera Phenix automated confocal microscope; Dr. Alec Heckert for sharing data analysis
893 pipeline and usage instructions; Dr. Hatice Kaya-Okur for valuable suggestions on Cut&Run
894 protocols. Dr. Alec Heckert, Dr. Andrew Belmont, Dr. John Lis, Dr. Jiang Xu, Dr. Max Staller, Dr.
895 Shasha Chong, and members of Tjian/Darzacq labs for helpful discussions and critical reading of
896 the manuscript. This work was supported by the NIH grant U54-CA231641-01 (to XD), and the
897 Howard Hughes Medical Institute (to RT). This work used the Vincent J. Coates Genomics
898 Sequencing Laboratory at UC Berkeley, supported by the NIH S10 OD018174 Instrumentation
899 Grant.

900

901 **Author contributions:** YC designed experiments with guidance from XD and RT. YC, CC, GD
902 and QZ performed experiments. YC drafted the original manuscript. CC, XD and RT reviewed
903 and edited the manuscript. XD and RT supervised the project.

904

905 **Competing interests:** RT and XD are co-founders of Eikon Therapeutics.

906

907 **References**

908 Anders S, Pyl PT, Huber W. 2014. HTSeq—a Python framework to work with high-throughput
909 sequencing data. *Bioinformatics* **31**:166–169. doi:10.1093/bioinformatics/btu638
910 Behera V, Evans P, Face CJ, Hamagami N, Sankaranarayanan L, Keller CA, Giardine B, Tan K,
911 Hardison RC, Shi J, Blobel GA. 2018. Exploiting genetic variation to uncover rules of
912 transcription factor binding and chromatin accessibility. *Nat Commun* **9**:782.
913 doi:10.1038/s41467-018-03082-6
914 Boijja A, Klein IA, Sabari BR, Dall'Agnese A, Coffey EL, Zamudio AV, Li CH, Shrinivas K, Manteiga
915 JC, Hannett NM, Abraham BJ, Afeyan LK, Guo YE, Rimel JK, Fant CB, Schuijers J, Lee TI,
916 Taatjes DJ, Young RA. 2018. Transcription factors activate genes through the phase
917 separation capacity of their activation domains. *Cell* **175**:1842.
918 doi:10.1016/j.cell.2018.10.042

919 Brent R, Ptashne M. 1985. A eukaryotic transcriptional activator bearing the DNA specificity of a
920 prokaryotic repressor. *Cell* **43**:729–736. doi:10.1016/0092-8674(85)90246-6
921 Brodaczewska KK, Szczylik C, Fiedorowicz M, Porta C, Czarnecka AM. 2016. Choosing the right
922 cell line for renal cell cancer research. *Mol Cancer* **15**:83. doi:10.1186/s12943-016-0565-
923 8
924 Brodsky S, Jana T, Mittelman K, Chapal M, Kumar DK, Carmi M, Barkai N. 2020. Intrinsically
925 Disordered Regions Direct Transcription Factor In Vivo Binding Specificity. *Mol Cell*
926 **79**:459-471.e4. doi:10.1016/j.molcel.2020.05.032
927 Burdach J, Funnell APW, Mak KS, Artuz CM, Wienert B, Lim WF, Tan LY, Pearson RCM, Crossley
928 M. 2014. Regions outside the DNA-binding domain are critical for proper in vivo
929 specificity of an archetypal zinc finger transcription factor. *Nucleic Acids Res* **42**:276–
930 289. doi:10.1093/nar/gkt895
931 Cho W-K, Spille J-H, Hecht M, Lee C, Li C, Grube V, Cisse II. 2018. Mediator and RNA polymerase
932 II clusters associate in transcription-dependent condensates. *Science* **361**:412–415.
933 doi:10.1126/science.aar4199
934 Chong S, Dugast-Darzacq C, Liu Z, Dong P, Dailey GM, Cattoglio C, Heckert A, Banala S, Lavis L,
935 Darzacq X, Tjian R. 2018. Imaging dynamic and selective low-complexity domain
936 interactions that control gene transcription. *Science* **361**:eaar2555.
937 doi:10.1126/science.aar2555
938 Chong S, Mir M. 2021. Towards Decoding the Sequence-Based Grammar Governing the
939 Functions of Intrinsically Disordered Protein Regions. *J Mol Biol* **433**:166724.
940 doi:10.1016/j.jmb.2020.11.023
941 Concordet J-P, Haeussler M. 2018. CRISPOR: intuitive guide selection for CRISPR/Cas9 genome
942 editing experiments and screens. *Nucleic Acids Res* **46**:W242–W245.
943 doi:10.1093/nar/gky354
944 Courey AJ, Tjian R. 1988. Analysis of Sp1 in vivo reveals multiple transcriptional domains,
945 including a novel glutamine-rich activation motif. *Cell* **55**:887–898. doi:10.1016/0092-
946 8674(88)90144-4
947 Darzacq X, Tjian R. 2022. Weak multivalent biomolecular interactions: a strength versus
948 numbers tug of war with implications for phase partitioning. *RNA* **28**:48–51.
949 doi:10.1261/rna.079004.121
950 Dobin A, Davis CA, Zaleski C, Schlesinger F, Drenkow J, Chaisson M, Batut P, Jha S, Gingeras TR.
951 2012. STAR: ultrafast universal RNA-seq aligner. *Bioinformatics* **29**:15–21.
952 doi:10.1093/bioinformatics/bts635
953 Edgar R, Domrachev M, Lash AE. 2002. Gene Expression Omnibus: NCBI gene expression and
954 hybridization array data repository. *Nucleic Acids Res* **30**:207–210.
955 doi:10.1093/nar/30.1.207
956 Gaur RK. 2014. Amino acid frequency distribution among eukaryotic proteins. *IIOAB J* **5**:6–11.
957 Gera T, Jonas F, More R, Barkai N. 2022. Evolution of binding preferences among whole-
958 genome duplicated transcription factors. *eLife* **11**:e73225. doi:10.7554/eLife.73225
959 Gnarra JR, Tory K, Weng Y, Schmidt L, Wei MH, Li H, Latif F, Liu S, Chen F, Duh FM. 1994.
960 Mutations of the VHL tumour suppressor gene in renal carcinoma. *Nat Genet* **7**:85–90.
961 doi:10.1038/ng0594-85

962 Grimm JB, Xie L, Casler JC, Patel R, Tkachuk AN, Falco N, Choi H, Lippincott-Schwartz J, Brown
963 TA, Glick BS, Liu Z, Lavis LD. 2021. A General Method to Improve Fluorophores Using
964 Deuterated Auxochromes. *Jacs Au* **1**:690–696. doi:10.1021/jacsau.1c00006
965 Grossman SR, Zhang X, Wang L, Engreitz J, Melnikov A, Rogov P, Tewhey R, Isakova A,
966 Deplancke B, Bernstein BE, Mikkelsen TS, Lander ES. 2017. Systematic dissection of
967 genomic features determining transcription factor binding and enhancer function. *Proc*
968 *Natl Acad Sci* **114**:E1291–E1300. doi:10.1073/pnas.1621150114
969 Hansen AS, Pustova I, Cattoglio C, Tjian R, Darzacq X. 2017. CTCF and cohesin regulate
970 chromatin loop stability with distinct dynamics. *eLife* **6**:e25776. doi:10.7554/eLife.25776
971 Hansen AS, Woringer M, Grimm JB, Lavis LD, Tjian R, Darzacq X. 2018. Robust model-based
972 analysis of single-particle tracking experiments with Spot-On. *eLife* **7**:e33125.
973 doi:10.7554/eLife.33125
974 Hanson J, Yang Y, Paliwal K, Zhou Y. 2017. Improving protein disorder prediction by deep
975 bidirectional long short-term memory recurrent neural networks. *Bioinformatics*
976 **33**:685–692. doi:10.1093/bioinformatics/btw678
977 Heckert A, Dahal L, Tjian R, Darzacq X. 2021. Recovering mixtures of fast diffusing states from
978 short single particle trajectories. bioRxiv. doi:10.1101/2021.05.03.442482
979 Hu C-J, Sataur A, Wang L, Chen H, Simon MC. 2007. The N-terminal transactivation domain
980 confers target gene specificity of hypoxia-inducible factors HIF-1alpha and HIF-2alpha.
981 *Mol Biol Cell* **18**:4528–4542. doi:10.1091/mbc.e06-05-0419
982 Jana T, Brodsky S, Barkai N. 2021. Speed–Specificity Trade-Offs in the Transcription Factors
983 Search for Their Genomic Binding Sites. *Trends Genet* **37**:421–432.
984 doi:10.1016/j.tig.2020.12.001
985 Janssens D, Henikoff S. 2019. CUT&RUN: Targeted in situ genome-wide profiling with high
986 efficiency for low cell numbers. *protocols.io*. https://www.protocols.io/view/cut-amp-
987 run-targeted-in-situ-genome-wide-profiling-zcpf2vn
988 Keith B, Johnson RS, Simon MC. 2012. HIF1α and HIF2α: sibling rivalry in hypoxic tumour growth
989 and progression. *Nat Rev Cancer* **12**:9–22. doi:10.1038/nrc3183
990 Kribelbauer JF, Rastogi C, Bussemaker HJ, Mann RS. 2019. Low-Affinity Binding Sites and the
991 Transcription Factor Specificity Paradox in Eukaryotes. *Annu Rev Cell Dev Biol* **35**:357–
992 379. doi:10.1146/annurev-cellbio-100617-062719
993 Langmead B, Trapnell C, Pop M, Salzberg SL. 2009. Ultrafast and memory-efficient alignment of
994 short DNA sequences to the human genome. *Genome Biol* **10**:R25. doi:10.1186/gb-
995 2009-10-3-r25
996 Li H, Handsaker B, Wysoker A, Fennell T, Ruan J, Homer N, Marth G, Abecasis G, Durbin R,
997 Subgroup 1000 Genome Project Data Processing. 2009. The Sequence Alignment/Map
998 format and SAMtools. *Bioinformatics* **25**:2078–2079.
999 Lim WF, Burdach J, Funnell APW, Pearson RCM, Quinlan KGR, Crossley M. 2016. Directing an
1000 artificial zinc finger protein to new targets by fusion to a non-DNA-binding domain.
1001 *Nucleic Acids Res* **44**:3118–3130. doi:10.1093/nar/gkv1380
1002 Liu Z, Lavis LD, Betzig E. 2015. Imaging Live-Cell Dynamics and Structure at the Single-Molecule
1003 Level. *Mol Cell* **58**:644–659. doi:10.1016/j.molcel.2015.02.033
1004 Los GV, Encell LP, McDougall MG, Hartzell DD, Karassina N, Zimprich C, Wood MG, Learish R,
1005 Ohana RF, Urh M, Simpson D, Mendez J, Zimmerman K, Otto P, Vidugiris G, Zhu J,

1006 Darzins A, Klaubert DH, Bulleit RF, Wood KV. 2008. HaloTag: A Novel Protein Labeling
1007 Technology for Cell Imaging and Protein Analysis. *ACS Chem Biol* **3**:373–382.
1008 doi:10.1021/cb800025k
1009 Love MI, Huber W, Anders S. 2014. Moderated estimation of fold change and dispersion for
1010 RNA-seq data with DESeq2. *Genome Biol* **15**. doi:10.1186/s13059-014-0550-8
1011 Ma J, Ptashne M. 1987. Deletion analysis of GAL4 defines two transcriptional activating
1012 segments. *Cell* **48**:847–853. doi:10.1016/0092-8674(87)90081-X
1013 McSwiggen DT, Hansen AS, Teves SS, Marie-Nelly H, Hao Y, Heckert AB, Umemoto KK, Dugast-
1014 Darzacq C, Tjian R, Darzacq X. 2019. Evidence for DNA-mediated nuclear
1015 compartmentalization distinct from phase separation. *eLife* **8**:e47098.
1016 doi:10.7554/eLife.47098
1017 Mermod N, O'Neill EA, Kelly TJ, Tjian R. 1989. The proline-rich transcriptional activator of
1018 CTF/NF-I is distinct from the replication and DNA binding domain. *Cell* **58**:741–753.
1019 doi:10.1016/0092-8674(89)90108-6
1020 Michel G, Minet E, Mottet D, Remacle J, Michiels C. 2002. Site-directed mutagenesis studies of
1021 the hypoxia-inducible factor-1α DNA-binding domain. *Biochim Biophys Acta BBA - Gene*
1022 *Struct Expr* **1578**:73–83. doi:10.1016/S0167-4781(02)00484-0
1023 Pellanda P, Dalsass M, Filipuzzi M, Loffreda A, Verrecchia A, Castillo Cano V, Thabussot H, Doni
1024 M, Morelli MJ, Soucek L, Kress T, Mazza D, Mapelli M, Beaulieu M-E, Amati B, Sabò A.
1025 2021. Integrated requirement of non-specific and sequence-specific DNA binding in
1026 Myc-driven transcription. *EMBO J* **40**:e105464. doi:10.15252/embj.2020105464
1027 Quinlan AR, Hall IM. 2010. BEDTools: a flexible suite of utilities for comparing genomic features.
1028 *Bioinforma Oxf Engl* **26**:841–842. doi:10.1093/bioinformatics/btq033
1029 Ramírez F, Ryan DP, Grüning B, Bhardwaj V, Kilpert F, Richter AS, Heyne S, Dündar F, Manke T.
1030 2016. deepTools2: a next generation web server for deep-sequencing data analysis.
1031 *Nucleic Acids Res* **44**:W160-165. doi:10.1093/nar/gkw257
1032 Rankin EB, Biju MP, Liu Q, Unger TL, Rha J, Johnson RS, Simon MC, Keith B, Haase VH. 2007.
1033 Hypoxia-inducible factor-2 (HIF-2) regulates hepatic erythropoietin in vivo. *J Clin Invest*
1034 **117**:1068–1077. doi:10.1172/JCI30117
1035 Raval RR, Lau KW, Tran MGB, Sowter HM, Mandriota SJ, Li J-L, Pugh CW, Maxwell PH, Harris AL,
1036 Ratcliffe PJ. 2005. Contrasting properties of hypoxia-inducible factor 1 (HIF-1) and HIF-2
1037 in von Hippel-Lindau-associated renal cell carcinoma. *Mol Cell Biol* **25**:5675–5686.
1038 doi:10.1128/MCB.25.13.5675-5686.2005
1039 Robinson JT, Thorvaldsdóttir H, Winckler W, Guttman M, Lander ES, Getz G, Mesirov JP. 2011.
1040 Integrative genomics viewer. *Nat Biotechnol* **29**:24–26. doi:10.1038/nbt.1754
1041 Rohs R, Jin X, West SM, Joshi R, Honig B, Mann RS. 2010. Origins of specificity in protein-DNA
1042 recognition. *Annu Rev Biochem* **79**:233–269. doi:10.1146/annurev-biochem-060408-
1043 091030
1044 Sabari BR, Dall'Agnese A, Boija A, Klein IA, Coffey EL, Shrinivas K, Abraham BJ, Hannett NM,
1045 Zamudio AV, Manteiga JC, Li CH, Guo YE, Day DS, Schuijers J, Vasile E, Malik S, Hnisz D,
1046 Lee TI, Cisse II, Roeder RG, Sharp PA, Chakraborty AK, Young RA. 2018. Coactivator
1047 condensation at super-enhancers links phase separation and gene control. *Science*
1048 **361**:eaar3958. doi:10.1126/science.aar3958

1049 Schödel J, Grampp S, Maher ER, Moch H, Ratcliffe PJ, Russo P, Mole DR. 2016. Hypoxia,
1050 Hypoxia-inducible Transcription Factors, and Renal Cancer. *Eur Urol* **69**:646–657.
1051 doi:10.1016/j.eururo.2015.08.007
1052 Schödel J, Oikonomopoulos S, Ragoussis J, Pugh CW, Ratcliffe PJ, Mole DR. 2011. High-
1053 resolution genome-wide mapping of HIF-binding sites by ChIP-seq. *Blood* **117**:e207–
1054 e217. doi:10.1182/blood-2010-10-314427
1055 Semenza GL. 2012. Hypoxia-Inducible Factors in Physiology and Medicine. *Cell* **148**:399–408.
1056 doi:10.1016/j.cell.2012.01.021
1057 Shen C, Beroukhim R, Schumacher SE, Zhou J, Chang M, Signoretti S, Kaelin WG. 2011. Genetic
1058 and Functional Studies Implicate HIF1α as a 14q Kidney Cancer Suppressor Gene. *Cancer*
1059 *Discov* **1**:222–235. doi:10.1158/2159-8290.CD-11-0098
1060 Smythies JA, Sun M, Masson N, Salama R, Simpson PD, Murray E, Neumann V, Cockman ME,
1061 Choudhry H, Ratcliffe PJ, Mole DR. 2019. Inherent DNA-binding specificities of the HIF-
1062 1α and HIF-2α transcription factors in chromatin. *EMBO Rep* **20**:e46401.
1063 doi:10.15252/embr.201846401
1064 Srivastava D, Mahony S. 2020. Sequence and chromatin determinants of transcription factor
1065 binding and the establishment of cell type-specific binding patterns. *Biochim Biophys*
1066 *Acta Gene Regul Mech* **1863**:194443. doi:10.1016/j.bbagrm.2019.194443
1067 Staller MV. 2022. Transcription factors perform a 2-step search of the nucleus. *Genetics*
1068 iyac111. doi:10.1093/genetics/iyac111
1069 Stark R, Brown G. 2011. DiffBind differential binding analysis of ChIP-Seq peak data. *R Package*
1070 *Version* **100**.
1071 Swiatek M, Jancewicz I, Kluebsoongnoen J, Zub R, Maassen A, Kubala S, Udomkit A, Siedlecki JA,
1072 Sarnowski TJ, Sarnowska E. 2020. Various forms of HIF-1α protein characterize the clear
1073 cell renal cell carcinoma cell lines. *IUBMB Life* **72**:1220–1232. doi:10.1002/iub.2281
1074 Tarasov A, Vilella AJ, Cuppen E, Nijman IJ, Prins P. 2015. Sambamba: fast processing of NGS
1075 alignment formats. *Bioinformatics* **31**:2032–2034. doi:10.1093/bioinformatics/btv098
1076 Testa A, Donati G, Yan P, Romani F, Huang TH-M, Viganò MA, Mantovani R. 2005. Chromatin
1077 immunoprecipitation (ChIP) on chip experiments uncover a widespread distribution of
1078 NF-Y binding CCAAT sites outside of core promoters. *J Biol Chem* **280**:13606–13615.
1079 doi:10.1074/jbc.M414039200
1080 Thorvaldsdóttir H, Robinson JT, Mesirov JP. 2013. Integrative Genomics Viewer (IGV): High-
1081 performance genomics data visualization and exploration. *Brief Bioinform* **14**:178–192.
1082 doi:10.1093/bib/bbs017
1083 Tjian R, Maniatis T. 1994. Transcriptional activation: a complex puzzle with few easy pieces. *Cell*
1084 **77**:5–8. doi:10.1016/0092-8674(94)90227-5
1085 Tokunaga M, Imamoto N, Sakata-Sogawa K. 2008. Highly inclined thin illumination enables clear
1086 single-molecule imaging in cells. *Nat Methods* **5**:159–161. doi:10.1038/nmeth1171
1087 Varma S, Cohen HJ. 1997. Co-transactivation of the 3' erythropoietin hypoxia inducible
1088 enhancer by the HIF-1 protein. *Blood Cells Mol Dis* **23**:169–176.
1089 doi:10.1006/bcmd.1997.0134
1090 Völkel S, Stielow B, Finkernagel F, Stiewe T, Nist A, Suske G. 2015. Zinc Finger Independent
1091 Genome-Wide Binding of Sp2 Potentiates Recruitment of Histone-Fold Protein Nf-y

1092 Distinguishing It from Sp1 and Sp3. *PLoS Genet* **11**:e1005102.
1093 doi:10.1371/journal.pgen.1005102
1094 Wallace EM, Rizzi JP, Han G, Wehn PM, Cao Z, Du X, Cheng T, Czerwinski RM, Dixon DD, Goggin
1095 BS, Grina JA, Halfmann MM, Maddie MA, Olive SR, Schlachter ST, Tan H, Wang B, Wang
1096 K, Xie S, Xu R, Yang H, Josey JA. 2016. A Small-Molecule Antagonist of HIF2α Is
1097 Efficacious in Preclinical Models of Renal Cell Carcinoma. *Cancer Res* **76**:5491–5500.
1098 doi:10.1158/0008-5472.CAN-16-0473
1099 Warnecke C, Zaborowska Z, Kurreck J, Erdmann VA, Frei U, Wiesener M, Eckardt K-U. 2004.
1100 Differentiating the functional role of hypoxia-inducible factor (HIF)-1alpha and HIF-
1101 2alpha (EPAS-1) by the use of RNA interference: erythropoietin is a HIF-2alpha target
1102 gene in Hep3B and Kelly cells. *FASEB J Off Publ Fed Am Soc Exp Biol* **18**:1462–1464.
1103 doi:10.1096/fj.04-1640fje
1104 Wei M-T, Chang Y-C, Shimobayashi SF, Shin Y, Strom AR, Brangwynne CP. 2020. Nucleated
1105 transcriptional condensates amplify gene expression. *Nat Cell Biol* **22**:1187–1196.
1106 doi:10.1038/s41556-020-00578-6
1107 Wenger RH, Stiehl DP, Camenisch G. 2005. Integration of oxygen signaling at the consensus
1108 HRE. *Sci Signal* **2005**:re12. doi:10.1126/stke.3062005re12
1109 Wu D, Potluri N, Lu J, Kim Y, Rastinejad F. 2015. Structural integration in hypoxia-inducible
1110 factors. *Nature* **524**:303–308. doi:10.1038/nature14883
1111 Xiang L, Chen K, Yan R, Li W, Xu K. 2020. Single-molecule displacement mapping unveils
1112 nanoscale heterogeneities in intracellular diffusivity. *Nat Methods* **17**:524–530.
1113 doi:10.1038/s41592-020-0793-0
1114 Xu R, Wang K, Rizzi JP, Huang H, Grina JA, Schlachter ST, Wang B, Wehn PM, Yang H, Dixon DD,
1115 Czerwinski RM, Du X, Ged EL, Han G, Tan H, Wong T, Xie S, Josey JA, Wallace EM. 2019.
1116 3-[(1S,2S,3R)-2,3-Difluoro-1-hydroxy-7-methylsulfonylindan-4-yl]oxy-5-
1117 fluorobenzonitrile (PT2977), a Hypoxia-Inducible Factor 2α (HIF-2α) Inhibitor for the
1118 Treatment of Clear Cell Renal Cell Carcinoma. *J Med Chem* **62**:6876–6893.
1119 doi:10.1021/acs.jmedchem.9b00719
1120 Zhang Y, Liu T, Meyer CA, Eeckhoute J, Johnson DS, Bernstein BE, Nusbaum C, Myers RM, Brown
1121 M, Li W, Liu XS. 2008. Model-based analysis of ChIP-Seq (MACS). *Genome Biol* **9**:R137.
1122 doi:10.1186/gb-2008-9-9-r137
1123

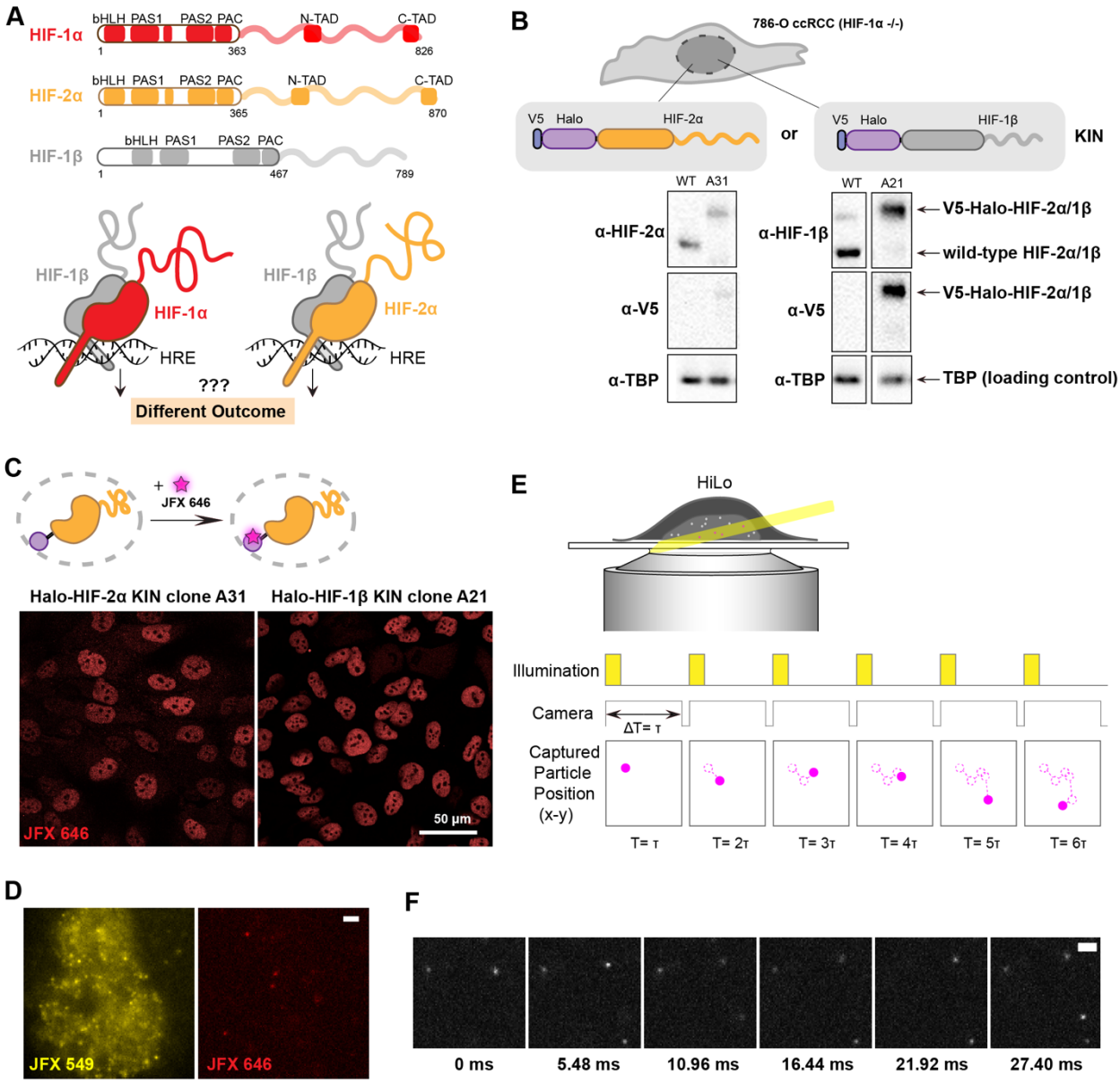

Figure 1. Endogenous tagging of HIFs in 786-O clear cell renal cell carcinoma (ccRCC) cells for fast single particle tracking (fSPT). (**A**) Schematic showing the similar domain organizations of HIFs (top) and the HRE-bound HIF α/β dimers (bottom). Disordered regions are represented as wavy lines. (**B**) Generation of Halo-KIN clones in the HIF-1α negative 786-O ccRCC line. Top: Halo-tagging scheme of HIF-2α (left) and HIF-1β (right). Bottom: Western blot of wild-type (WT) 786-O cells and homozygously tagged knock-in clones (A31 and A21). See Figure 1—figure supplement 2 for uncropped images. (**C**) Halo-tagged HIF-2α and HIF-1β show predominant nuclear localization. Top: schematic of labeling Halo-tagged proteins in live cells with cell-permeable Halo-binding JFX646 dye. Bottom: representative images of Halo-HIF-2α (left) and

1133 Halo-HIF-1β (right) clones labeled with 500 nM JFX646 (**D**) representative images showing the
1134 same cell labeled with a high concentration of JFX549 dye for localizing the nucleus in one
1135 channel (left) and labeled sparsely with JFX646 dye for tracking individual molecules in another
1136 channel (right). Scale bar = 2 μm. (**E**) Graphical illustration of fSPT capturing trajectories of moving
1137 particles. Top: highly inclined and laminated optical sheet illumination (HiLo). Bottom: Illumination
1138 and camera sequence with corresponding particle position at each frame (solid magenta dots).
1139 Particle's past positions (dashed magenta circles) are connected with dotted magenta lines to
1140 show the particle's trajectory. Scale bar = 2 μm. (**F**) Actual data showing detection of Halo-HIF-
1141 2α protein molecules at 5.48 ms frame rate.

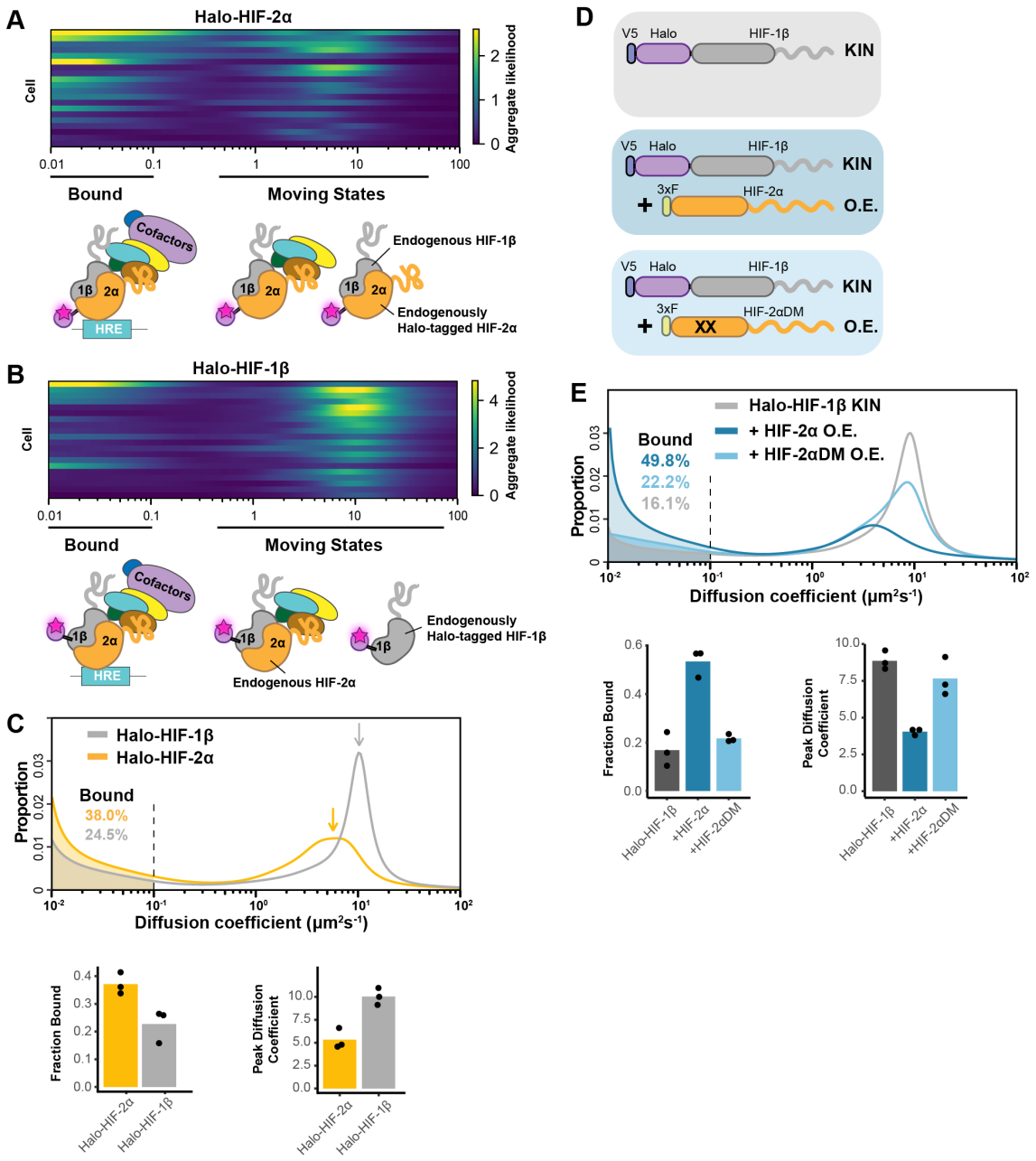

Figure 2. fSPT sensitively detects molecules in a range of states. (**A-B**) Likelihood of diffusion coefficients based on a model of regular Brownian motion with localization error (RBME) (Heckert et al., 2021), for (A) Halo-HIF-2α, clone A31 and (B) Halo-HIF-1β, clone A21, with drawing illustrating bound and different hypothetical moving states: complexes, dimer and monomer. Each row represents data collected from one cell. 0.1 μm^2/sec is used as the cut-off for bound versus free. (**C**) Top: proportion of molecules as a function of their diffusion coefficients (posterior mean occupations for a state array (Heckert et al., 2021)) evaluated on trajectories across all cells measured for each KIN line (Halo-HIF-2α, clone A31 and Halo-HIF-1β, clone A21). Compared to

1150 HIF-2α, HIF-1β has less bound fraction (grey versus yellow shaded areas) and faster diffusion
1151 coefficient (grey versus yellow arrows). Bottom: Summary of the bound fraction (left) and peak
1152 diffusion coefficient (right) for the two clones. Each bar represents the averaged value from three
1153 independent measurements on different days (black dots). (**D-E**) Over-expressing HIF-2α, but
1154 not a dimerization mutant form, in the Halo-HIF-1β knock-in (KIN) line increases HIF-1β binding
1155 and decreases its diffusion coefficient. (D) schematic illustrating the parental Halo-HIF-1β KIN
1156 cells (grey background) and cells stably over-expressing (O.E.) either the wild type (darker blue
1157 background) or a dimerization mutant (DM, black crosses, lighter blue background) form of HIF-
1158 2α. (E) Top: Proportion of molecules as a function of diffusion coefficient measured for HIF-1β in
1159 Halo-HIF-1β KIN cells (grey) and in Halo-HIF-1β KIN cells overexpressing HIF-2α (WT, dark blue
1160 background, or dimerization mutant (HIF-2αDM), light blue). Shaded areas indicate bound
1161 fraction. Bottom: Bar plot of the average value (bar height) of the bound fraction (left) and peak
1162 diffusion coefficient (right) calculated from three independent measurements (black dots) for each
1163 condition.

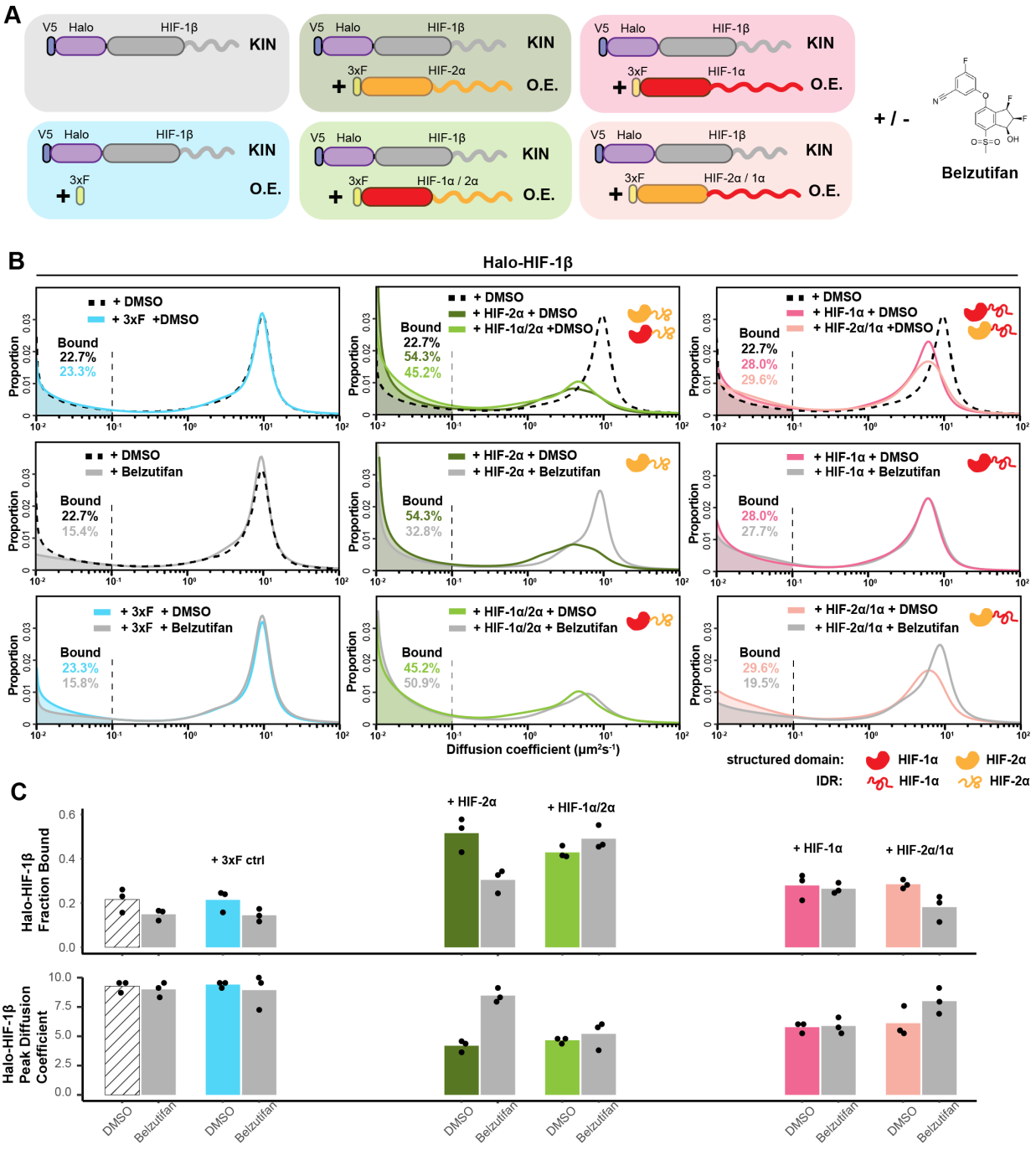

Figure 3. HIF-α increases HIF-1β binding and decreases HIF-1β diffusion coefficient through dimerization, in an IDR-dependent manner. (**A**) Schematic of evaluating Halo-HIF-1β behavior with genetic and small-molecule perturbation. Parental Halo-HIF-1β knock-in (KIN) cells (grey background) and cells stably overexpressing (O.E.) either a certain form of HIF-α (WT or domain swap, HIF-1α, red, HIF-2α, orange. Disordered regions are represented as wavy lines.) (various colored background) or a 3xFLAG tag only control (blue background) are used, with and without

1170 0.2 μM Belzutifan (HIF-2α/1β dimerization inhibitor) treatment. (**B**) Proportion of Halo-HIF-1β
1171 molecules as a function of diffusion coefficient measured in various conditions outlined in (A) Top
1172 row: DMSO only, showing overexpressing α subunit can change HIF-1β behavior. Cells over-
1173 expressing the α subunit variants containing HIF-2α disordered region (orange curly line) have a
1174 stronger effect (middle, HIF-2α and HIF-1α/2α,) compared to those containing HIF-1α disordered
1175 region (right, HIF-1α and HIF-2α/1α). Middle and Bottom rows: proportions of HIF-1β as a function
1176 of diffusion coefficient, measured in each of the 6 cell lines with Belzutifan treatment are compared
1177 to the DMSO control. Changes caused by overexpressing an α subunit can be specifically
1178 reverted by Belzutifan treatment for cell lines expressing an α subunit variant that contains the
1179 HIF-2α structured domain (orange globule). (**C**) Summary of the average bound fractions (top)
1180 and peak diffusion coefficient (bottom) for all 12 conditions, with black dots indicating values from
1181 each of the three individual measurements.

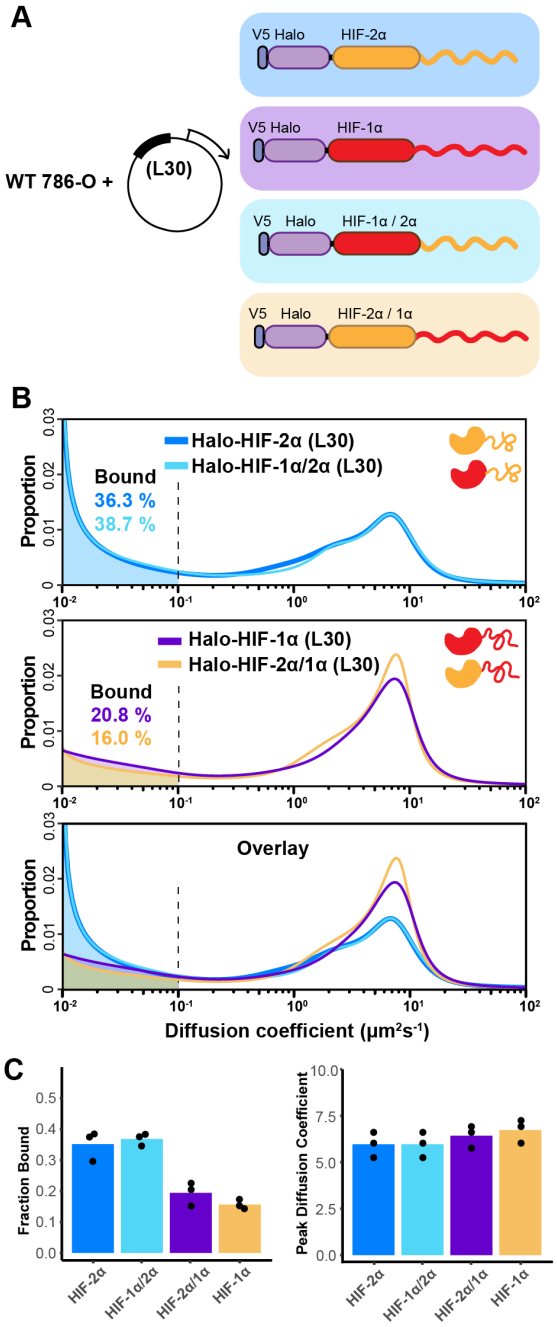

Figure 4. The IDR governs HIF-α molecular dynamics and binding characteristics. (**A**) Schematic representation of different HIF (WT and domain-swapped) being weakly and stably overexpressed with an L30 promoter and tracked in WT 786-O cells. (**B**) Proportion of molecules as a function of diffusion coefficient for every tracked protein in (A). Top: overlapping distribution curves shows almost identical behavior between Halo-HIF-2α (dark blue curve) and Halo-HIF-1α/2α (light blue curve). Middle: similar behavior between Halo-HIF-1α (purple curve) and Halo-HIF-2α/1α (yellow curve), bottom: overlay of all four curves shows very different behavior between

1189 proteins containing 1α versus 2α IDR. (**C**) Bar plot comparing the average bound fraction (left)
1190 and peak diffusion coefficient (right) for cells in (B), with black dots indicating values from three
1191 independent measurements.

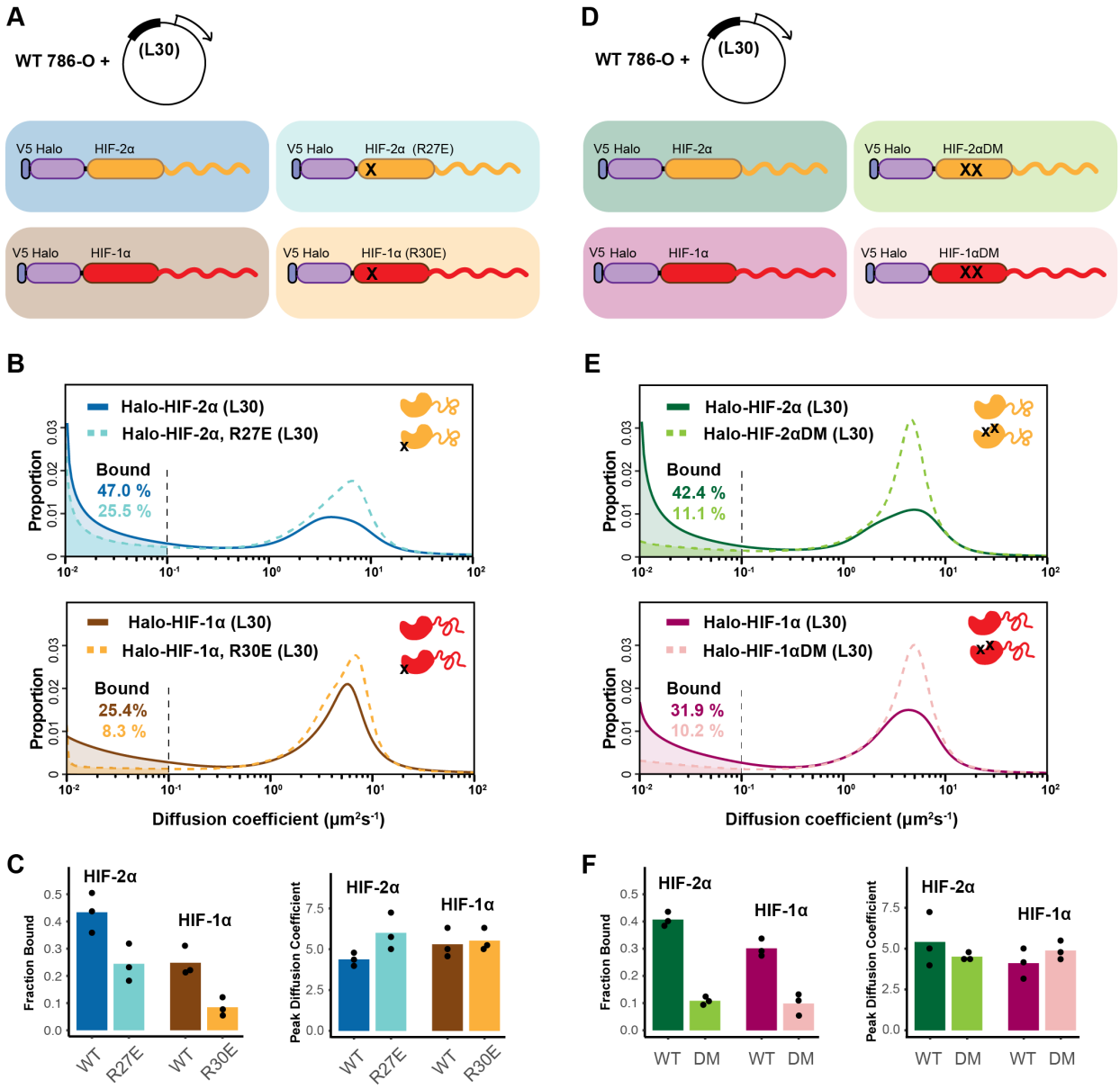

Figure 5. HIF-α IDR alone is not sufficient for binding. (**A-C**) Mutation in DBD reduces the bound fraction for both HIF-α isoforms. (A) Schematic representation of weakly overexpressing and tracking wild type and DBD mutant (R27E or R30E, black cross) forms of HIF-1α or -2α, using the same L30 expression system as in Figure 4. (B) Proportion of molecules as a function of diffusion coefficient for tracked protein listed in (A). (C) Bar plot summarizes the average value (bar height) of the bound fraction (left) and peak diffusion coefficient (right) of three independent measurements (black dots). (**D-F**) Mutations in the dimerization domain reduce the bound fraction for both HIF-α isoforms but do not change their diffusion coefficient. (D) Schematic representation of weakly over-expressing and tracking wild type and dimerization-mutant (DM, two black crosses) forms of Halo-HIF-1α or -2α, using the L30 expression system. (E) Proportion of

1202 molecules as a function of diffusion coefficient for tracked protein in (D). (F) Summary of the
1203 average value (bar height) of the bound fraction (left) and peak diffusion coefficient (right) for all
1204 four proteins with black dots indicating values from three independent measurements.

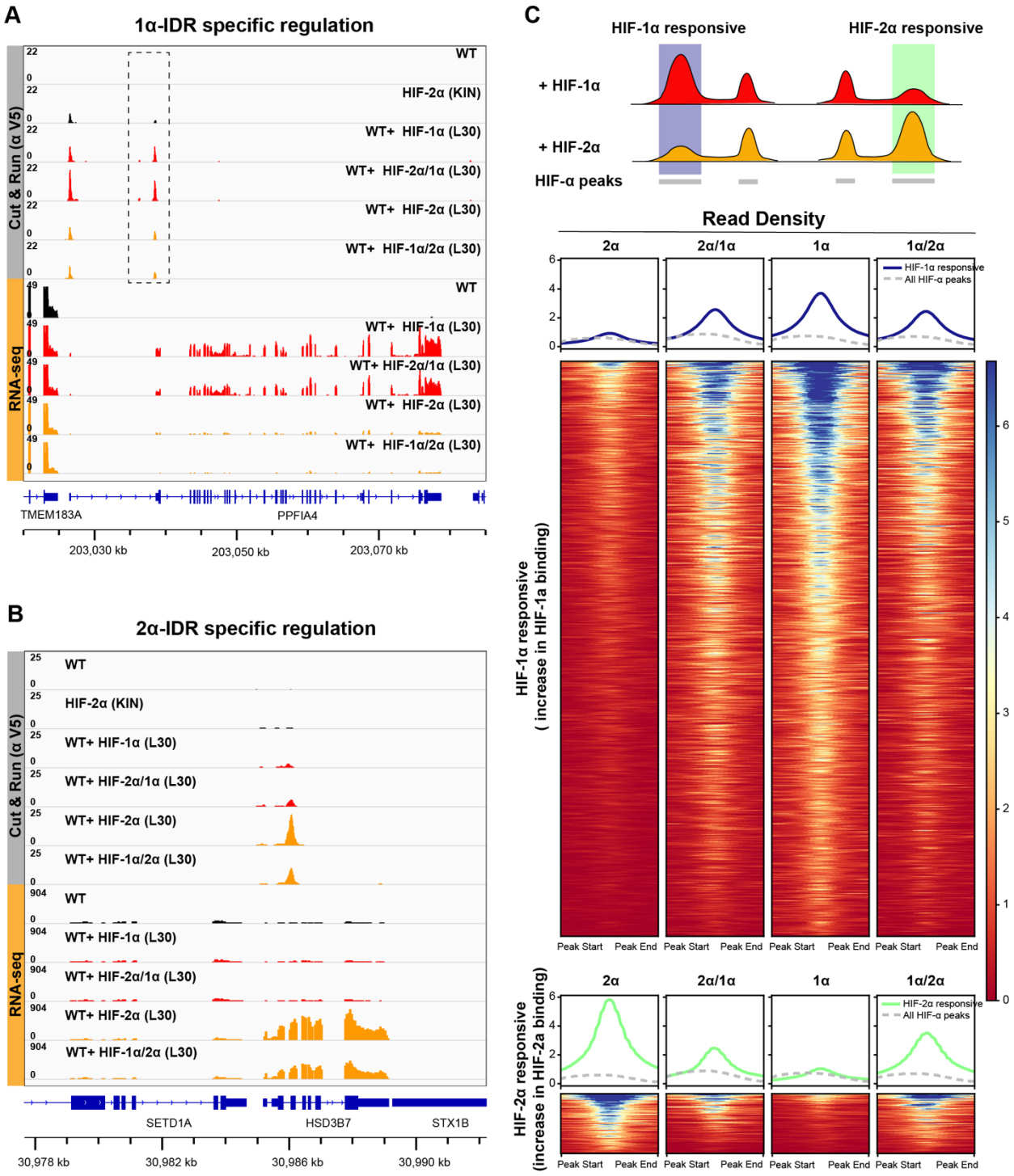

Figure 6. HIF-α IDR contributes to isoform-specific chromatin binding preferences and activation of isoform-specific HIF target genes. (**A-B**) Genome browser view of anti-V5 Cut&Run and RNA-seq results on WT cells, Halo-HIF-2α KIN cells and cells expressing different Halo-tagged HIF-α variants driven by an L30 promoter, showing IDR-specific regulation. (A) An example of genes that are preferentially bound (dashed box) and specifically activated by HIF-1α, as well as by HIF-

1210 2α/1α. (B) An example of genes that are preferentially bound and specifically activated by HIF-
1211 2α, as well as by HIF-1α/2α. (**C**) Genome-wide analysis of contribution of DBD or IDR on isoform-
1212 specific binding with Cut&Run data. Top: Schematic showing definition of HIF-1α and HIF-2α
1213 responsive regions. Regions that show increased binding when overexpressing Halo-tagged HIF-
1214 1α compared to when overexpressing Halo-tagged HIF-2α are defined as HIF-1α responsive
1215 regions (purple highlight). Regions that show increased binding when overexpressing Halo-
1216 tagged HIF-2α compared to when overexpressing HIF-1α are defined as HIF-2α responsive
1217 regions (green highlight). Bottom: heatmap and pile-up results (blue curves for HIF-1α responsive
1218 regions and green curves for HIF-2α responsive regions) on binding strength at all HIF-1α
1219 responsive regions or HIF-2α responsive regions when cells overexpressing either Halo-tagged
1220 HIF-2α, -2α/1α, -1α, or -1α/2α. Pile-up enrichment results at all HIF binding sites (dashed grey
1221 curves) are used as control.
1222

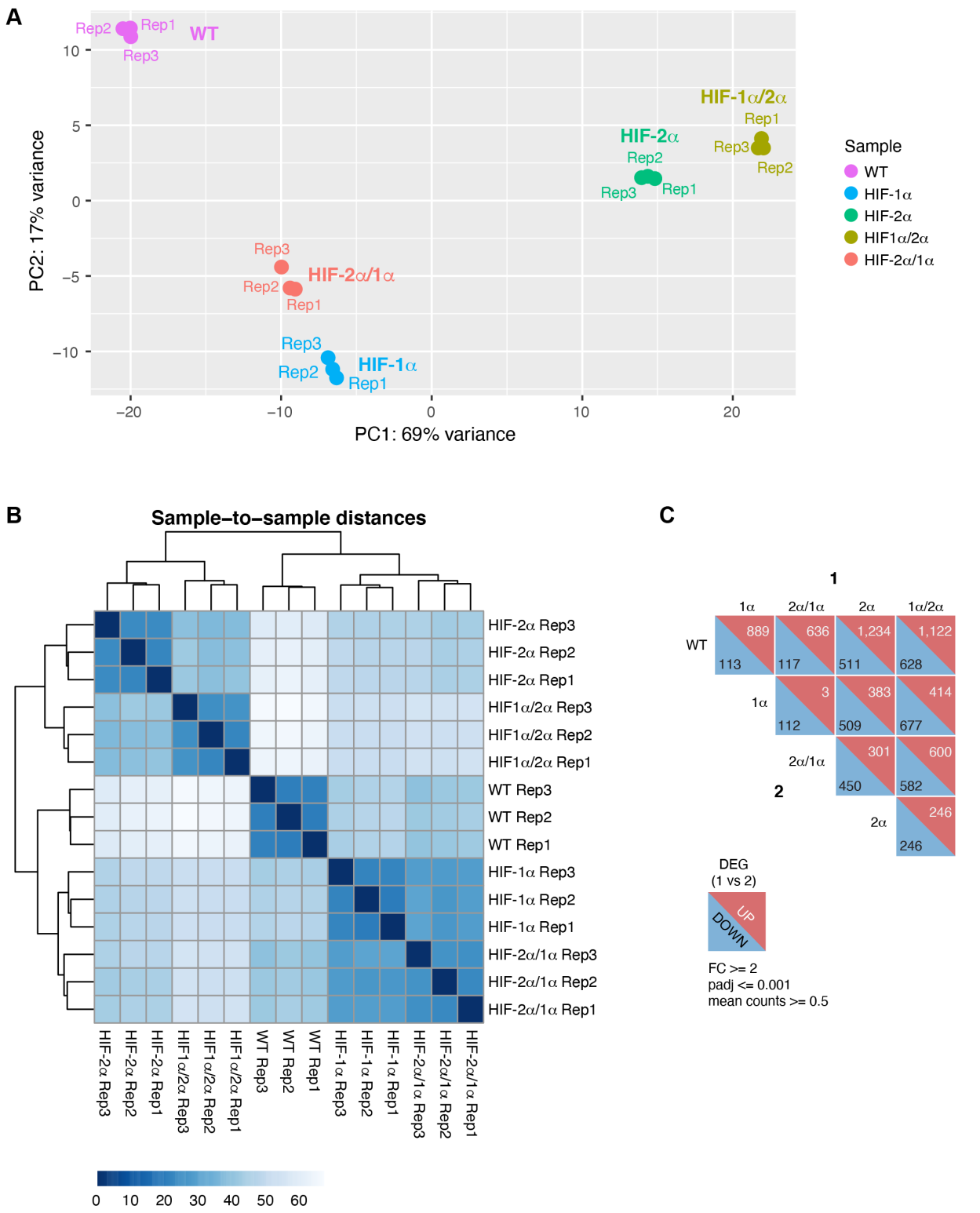

1223 **Figure 7.** RNA-seq analysis shows HIF-α isoform-specific gene regulation is IDR-dependent. (**A-**
1224 **B**) PCA analysis (A) and Clustering (B) of RNA-seq results performed on WT 786-O cells, and

1225 cells expressing Halo-tagged HIF-α variants driven by an L30 promoter. HIF-α variants sharing
1226 the same IDR (-1α and -2α/1α or -2α and -1α/2α) have similar gene expression profiles. (**C**)
1227 DESeq2 output summarizing pair-wise comparison of the number of differentially expressed
1228 genes (DEG) in WT cells and cells over-expressing various HIF-α forms.
1229

1230

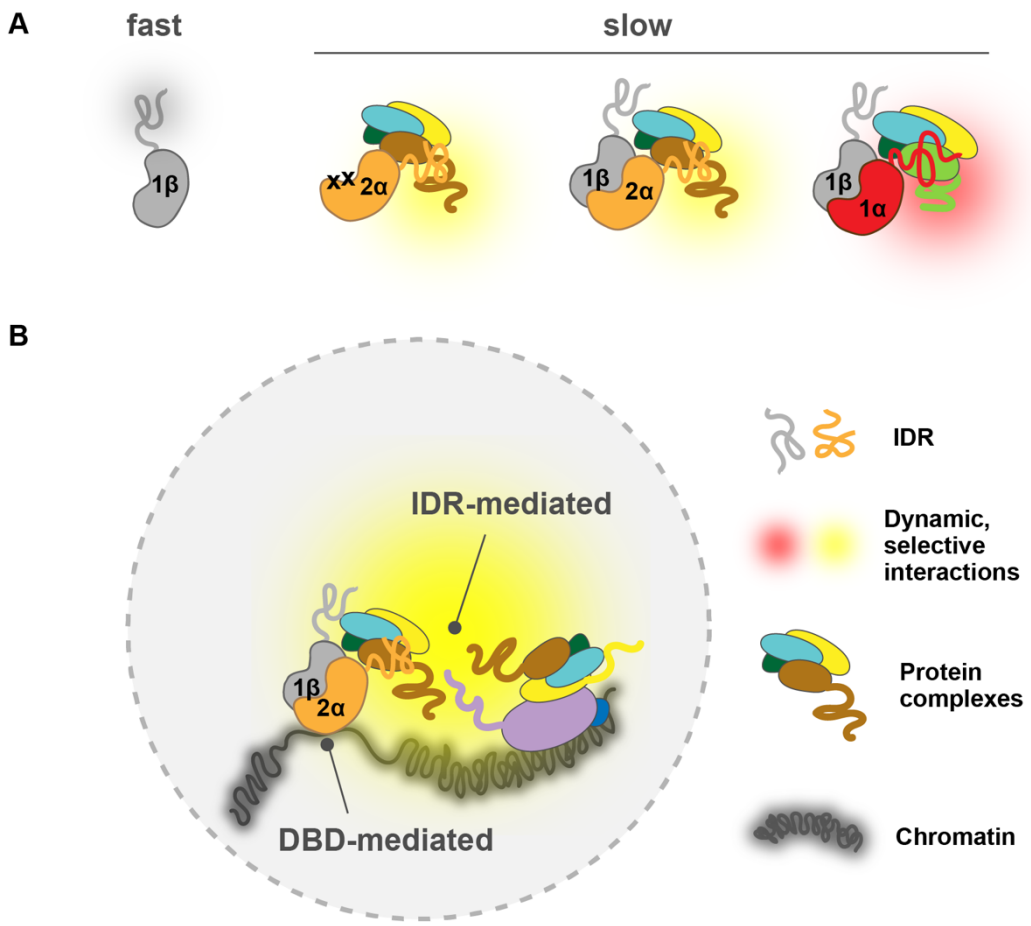

1231 **Figure 8.** A model for IDR-mediated nuclear search and chromatin binding. (**A**) The HIF-α IDR
1232 determines its slow motion of both the HIF-α monomer and HIF-α/β dimer, likely by HIF-α IDR
1233 mediated interactions with nuclear macromolecules. For HIF-α, the IDR thus determines its slow
1234 motion regardless of its dimerization status. For HIF-1β, dimerization slows it down due to extra
1235 interactions (yellow and red clouds) brought by HIF-α IDR. (**B**) HIF-chromatin engagement
1236 comprises two components: DBD- and IDR-mediated interactions. As an obligated dimer, the
1237 DBD and the dimerization domain are both necessary for HIF binding, but the IDR determines the
1238 bound fraction, possibly via its interaction with nearby macromolecules, including other proteins
1239 and/or nucleic acids (DNA and/or RNA).

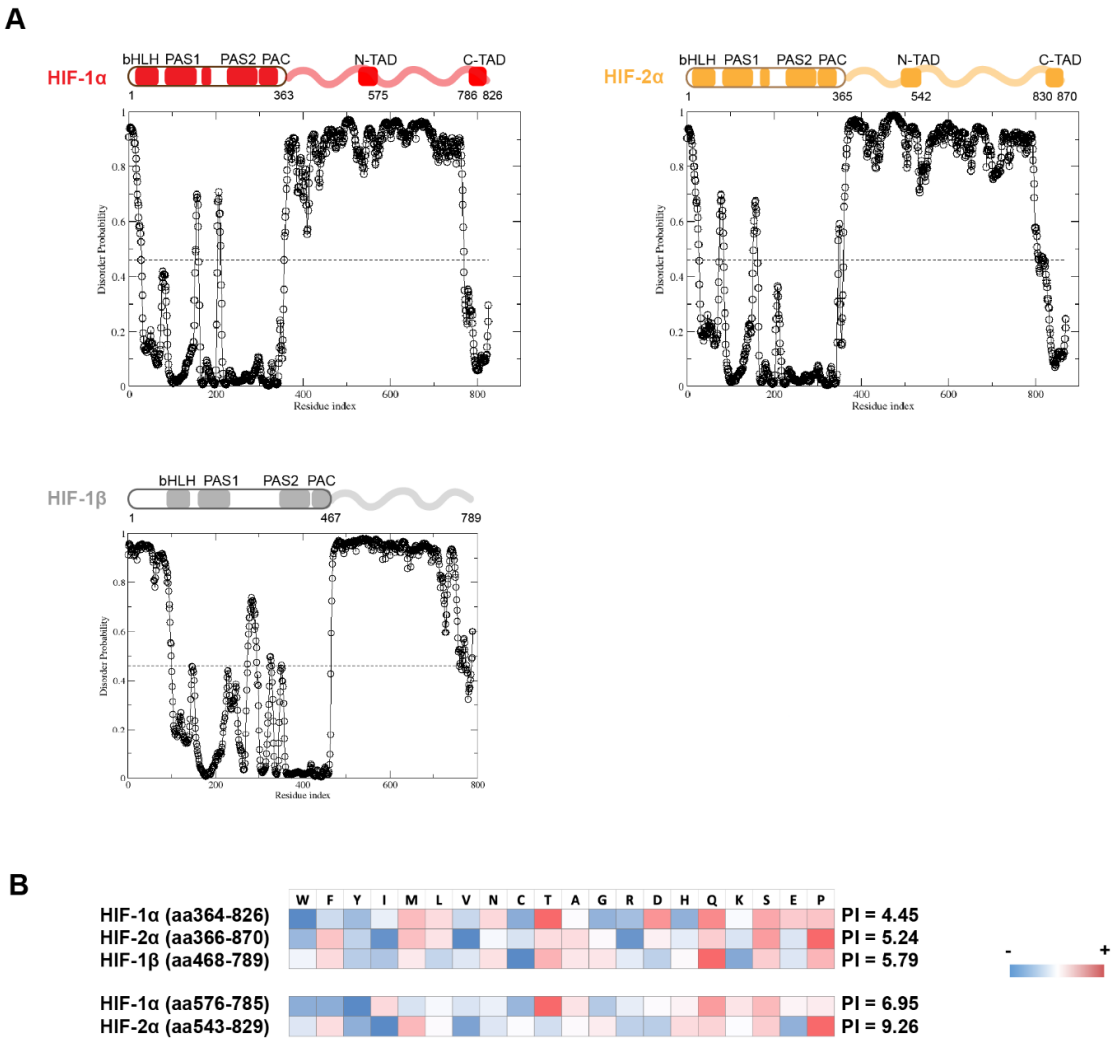

Figure 1—figure supplement 1. Domain analysis of HIFs. (**A**) Disorder propensity of HIF-1α, -2α and -1β, predicted by SPOT-Disorder (Hanson et al., 2017). High values indicate higher disorder propensity. (**B**) HIF-1α and HIF-2α IDRs have different amino acid composition biases. The relative enrichment for each amino acid is calculated by comparison with the average amino acid composition of non-membrane proteins in vertebrates (Gaur, 2014), and color coded, with red indicating relative high enrichment and blue indicating relative depletion. The IDR segments between the N-TAD and C-TAD are especially different between HIF-1α and HIF-2α in terms of acidity (bottom).

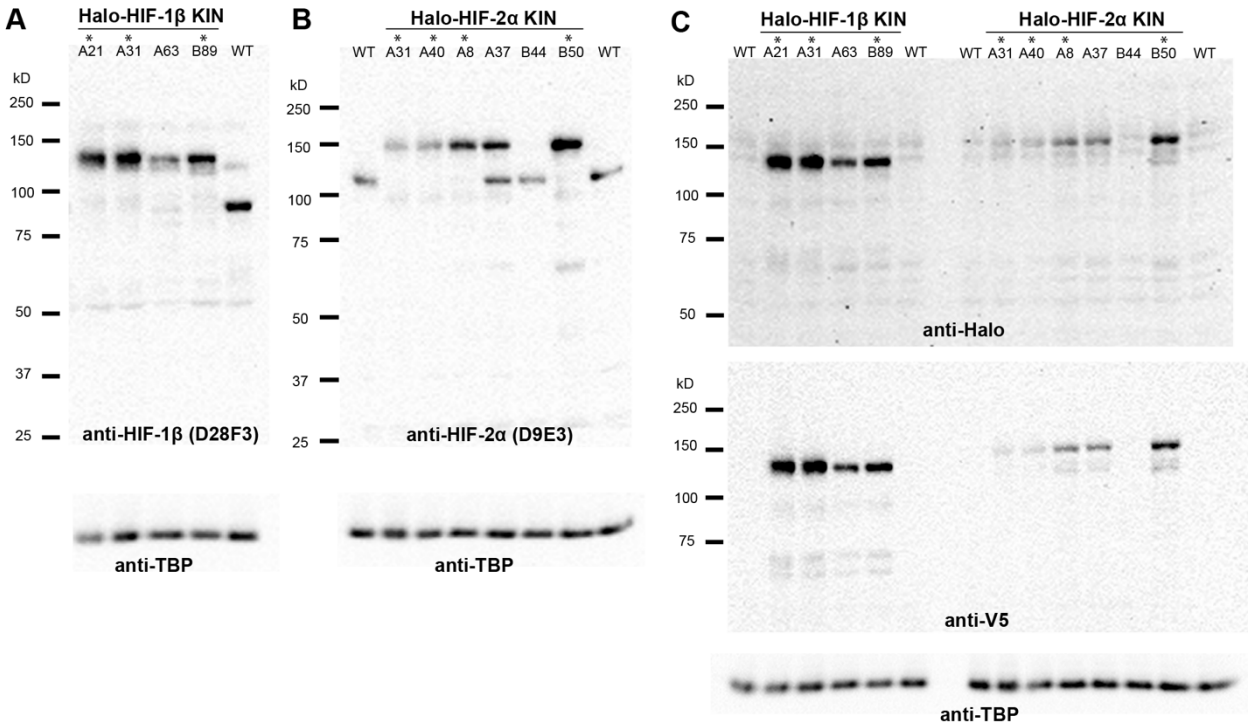

Figure 1—figure supplement 2. Verification of endogenous tagging of HIFs in 786-O ccRCC cells. (**A**) (**B**) (**C**) Uncropped images of western blot of wild-type (WT) 786-O cells and homozygously tagged knock-in clones (*). See Figure 1—figure supplement 2-source data 1-6 for raw image files. (A) HIF-2α protein is detected in WT and various KIN clones with a Rabbit monoclonal antibody against HIF-2α (Cell Signaling, D9E3), membranes were stripped and reblotted for TBP for loading control. (B) HIF-1β protein is detected in WT and various KIN clones with a Rabbit monoclonal antibody against HIF-1β (Cell Signaling, D28F3), membranes were stripped and reblotted for TBP for loading control. (C) Various HIF-2α and HIF-1β KIN clones are loaded on the same gel and probed for tagged protein levels using an anti-Halo antibody (top); the membrane was stripped and reblotted for TBP for loading control, then stripped again and reblotted for V5 tag. Halo-HIF-1β is generally expressed at a much higher level than Halo-HIF-2α, as shown by the detected Halo or V5 level.

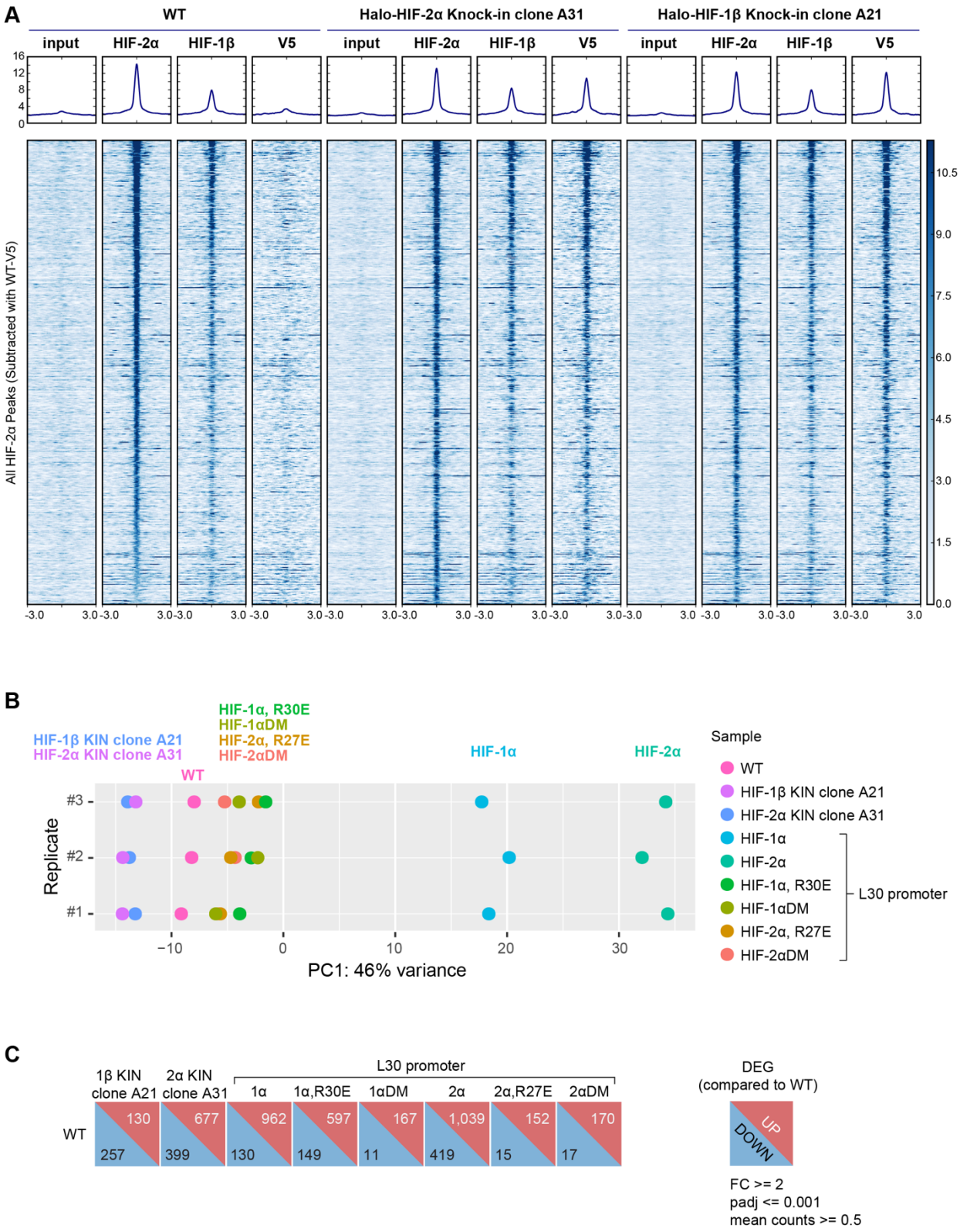

1262 **Figure 1—figure supplement 3.** HIF genome-wide binding and RNA expression profiles after
1263 gene-editing and genetic modification. (**A**) HeatMap of the ChIP-seq experiments comparing

1264 binding profiles of HIF-2α and HIF-1β in WT or KIN clones. ChIP-Seq read counts (Reads Per
1265 Genomic Content) are plotted at MAC2-called HIF-2α peak regions (across all cell lines and
1266 subtracted of V5 peaks called in WT 786-O cells) centered around the peak. (**B**) Principle
1267 Component Analysis (PCA) on RNA-seq data from WT, Halo-HIF-2α and Halo-HIF-1β KIN
1268 clones, and WT cells over-expressing various HIF-α forms driven by an L30 promoter. Only the
1269 first principle component (largest variance) is shown for three biological replicates. Both KIN
1270 cells (HIF-1β KIN and HIF-2α KIN) and cells overexpressing inactive HIF-α mutants (HIF-1α
1271 R30E, HIF-1αDM, HIF-2α R27E, HIF-2αDM) are close to WT cells. In contrast, cells
1272 overexpressing functional HIF-α (HIF-1α and HIF-2α) show farther deviations from WT cells. (**C**)
1273 DESeq2 output summarizing the number of differentially expressed genes (DEG) in KIN cell
1274 lines and cells over-expressing various HIF-α forms, compared to WT cells.
1275

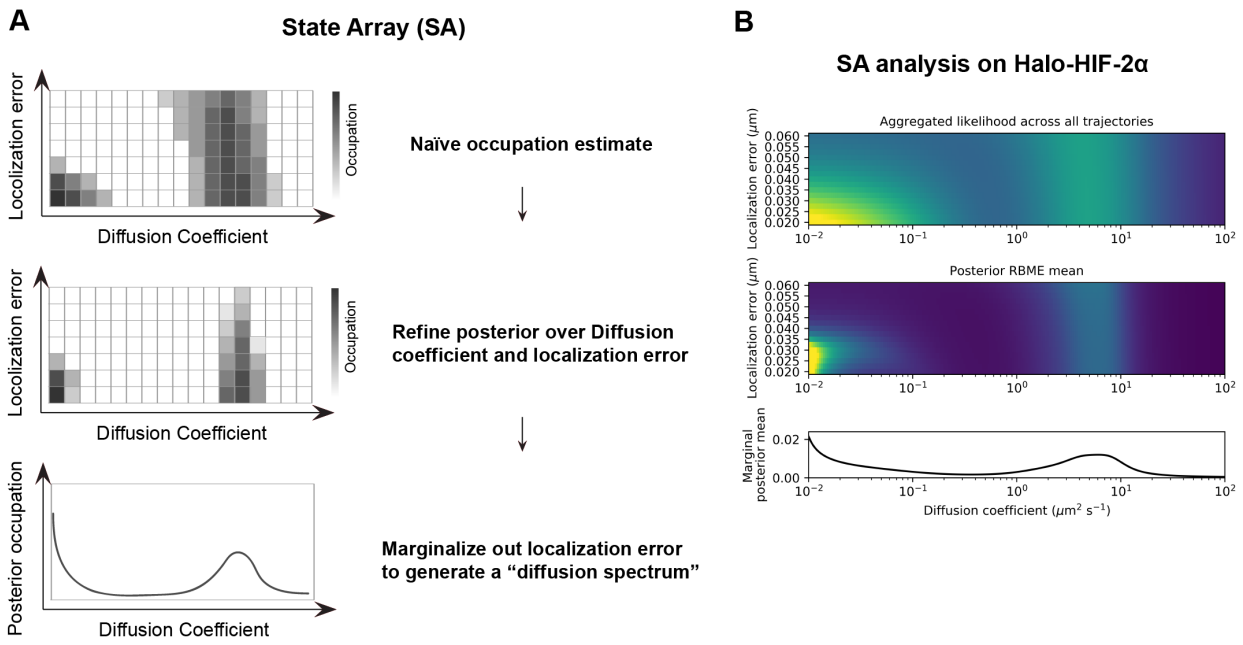

Figure 2—figure supplement 1. State Array (SA) analysis on fSPT data. (**A**) Schematic of the SA workflow. Top: Step 1, naïve occupation is estimated for each state in an array of states spanning different localization errors (y axis) and diffusion coefficients (x-axis), by simply applying the RBME likelihood estimation on trajectory data. Middle: Step 2, refining posterior over diffusion coefficient and localization error. Bottom: Step 3, marginalizing out localization error to generate the posterior occupation (i.e. proportion of molecules, y-axis) as a function of diffusion coefficients (x-axis) to get the final "diffusion spectrum". (**B**) Real example of SA analysis results from each of the three steps. Trajectory data are collected from Halo-HIF-2α KIN clone A31, the same data presented in Figure 2C.

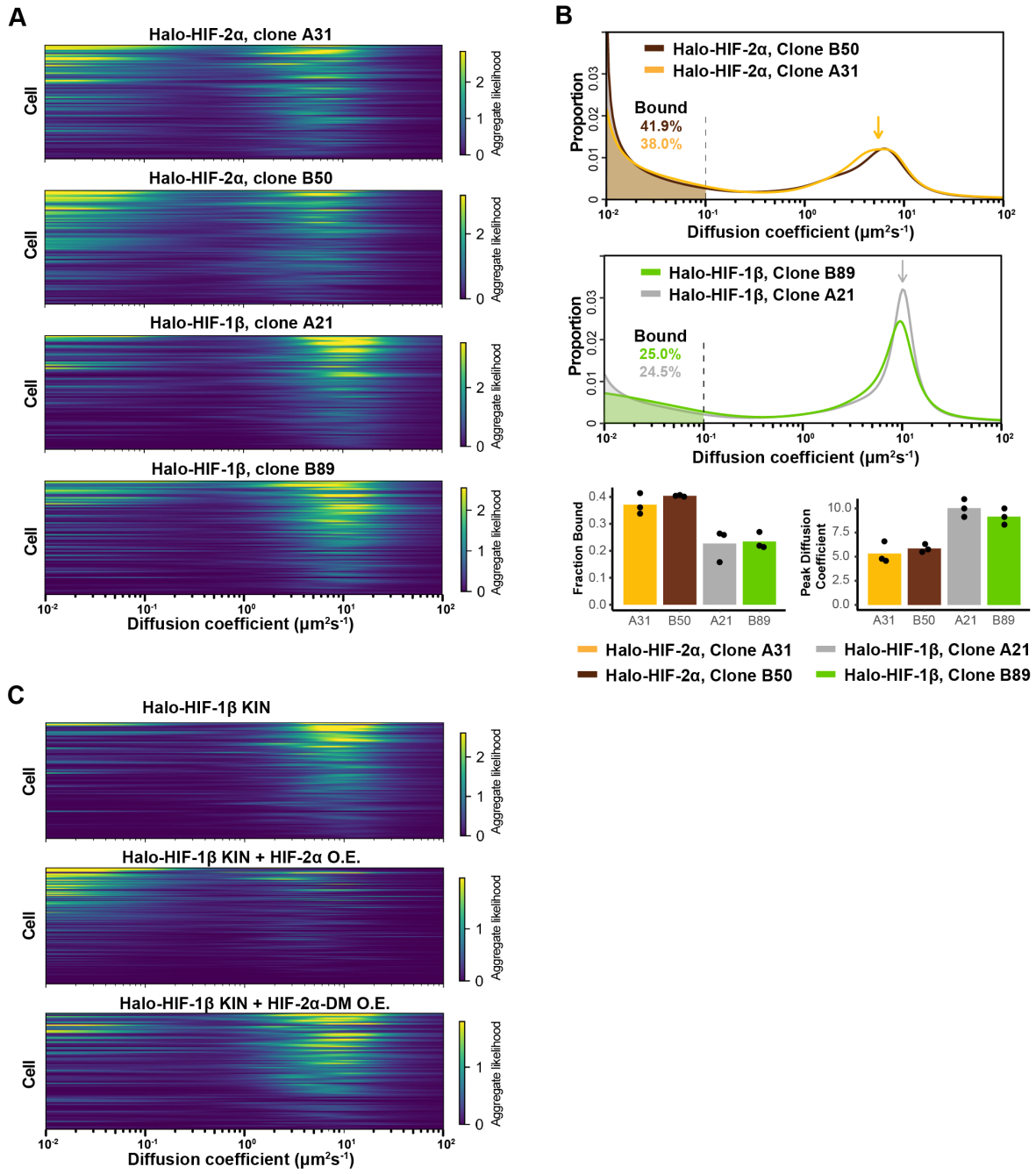

Figure 2—figure supplement 2. HIF-1β behavior is distinct from HIF-2α and changes as 1β-to-2α stoichiometry changes. (**A**) RBME likelihood of diffusion coefficient in individual cells for four Halo-HIF-2α or Halo-HIF-1β KIN clonal lines. (**B**) Top and middle: proportion of molecules as a function of their diffusion coefficients (posterior mean occupations for a state array) evaluated on trajectories across all cells measured for additional Halo-HIF KIN line showing reproducible results in different KIN clones (Top, clone A31 and B50 for Halo-HIF-2α KIN and middle, clone A21 and B89 for Halo-HIF-1β KIN). Data for clone A21 and A31 are replotted from Figure 2.

1292 Bottom: Summary of the bound fraction (left) and peak diffusion coefficient (right) for all four cell
1293 lines. Each bar represents the average of three independent measurements on different days
1294 (black dots). (**C**) RBME likelihood of diffusion coefficient obtained for individual cells in either Halo-
1295 HIF-1β KIN cells (top) or Halo-HIF-1β KIN cells overexpressing HIF-2α (WT, middle or DM,
1296 bottom).
1297

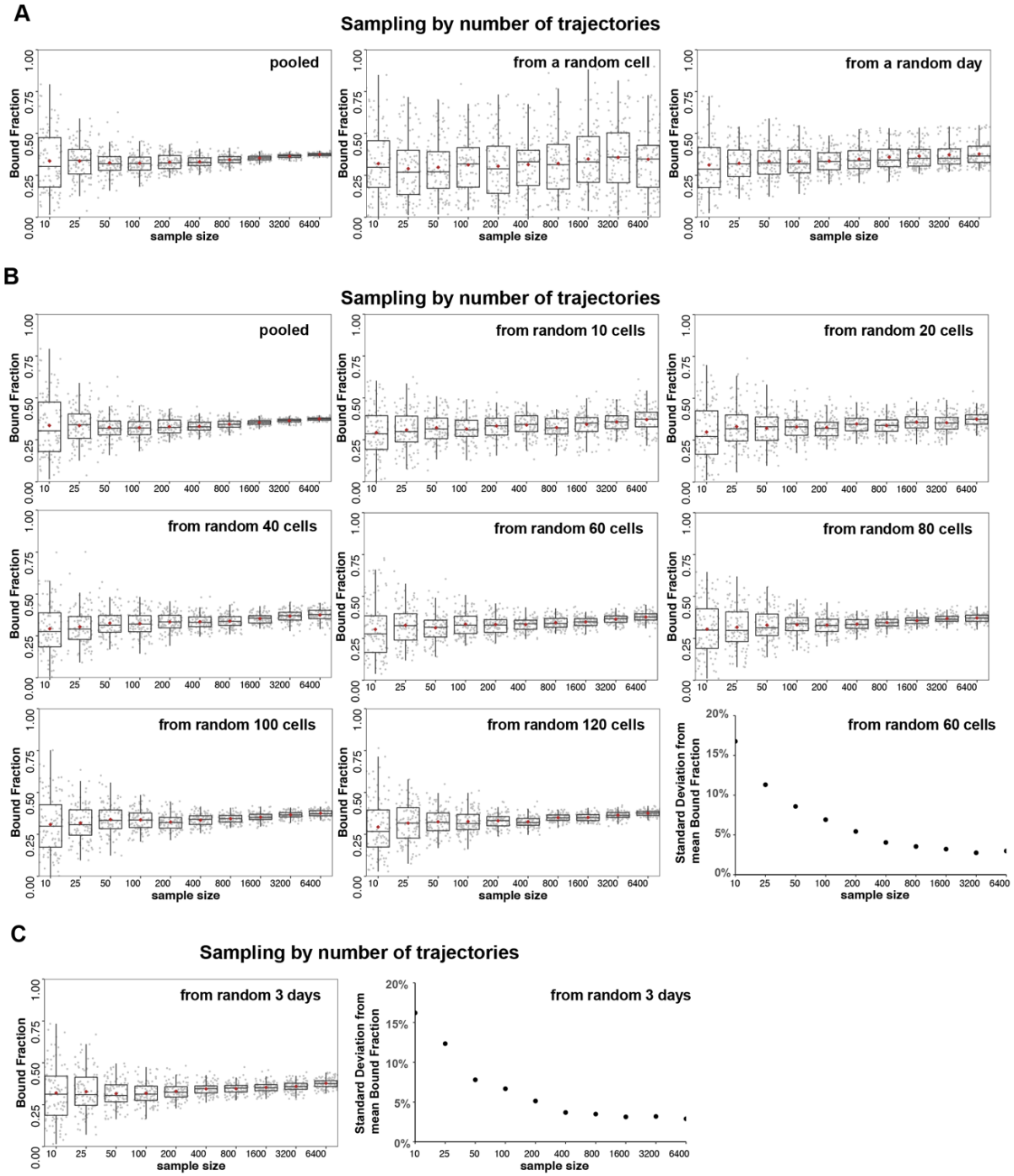

1298 **Figure 2—figure supplement 3.** Analysis of source of variation by bootstrapping. (**A-C**) Halo-
1299 HIF-2α trajectories imaged from KIN clone A31 are used for subsampling and SA analysis.
1300 Sampling (with replacement) was done by the number of trajectories (sample size = 10, 25, 50,
1301 100, 200, 400, 800, 1600, 3200 and 6400), then analyzed with SA and the estimated bound
1302 fraction was plotted as a dot. For each sample size, 100 replicates were performed and plotted

as 100 dots with box plot on top showing variation and the brown diamond indicating the mean. (A) The main source of variation is cell-to-cell variability, followed by day-to-day (i.e. replicate-to-replicate) variability. Left: Each sampling was drawn from pooled trajectories of 243 movies (cells) taken on 11 different days. As the trajectory size increases, the results converge. Middle: Each sample was drawn from a single cell that was randomly selected from 243 cells. Increasing the number of trajectories does not improve the variance. Right: Each sample was drawn from all the trajectories collected on a single day that was randomly selected from the 11 different days. Increasing the number of trajectories improves the variance but some variation remains. (B) Different number of cells are used for sampling to evaluate variation. For each graph, each sample was drawn from N unique cells as indicated (N = a pooled of 243 cells; or 10, 20, 40, 60, 80, 100, 120 randomly selected from the pool of 243 cells). Replicates done with more than 60 random cells can achieve a standard deviation less than 5% when the total trajectory number is over 800. (C) A random pool of trajectories from 3 different days are used for each draw, showing that an estimation with data randomly collected from 3 independent replicates (i.e. days) can achieve a standard deviation less than 5% when the total trajectory number is over 800.

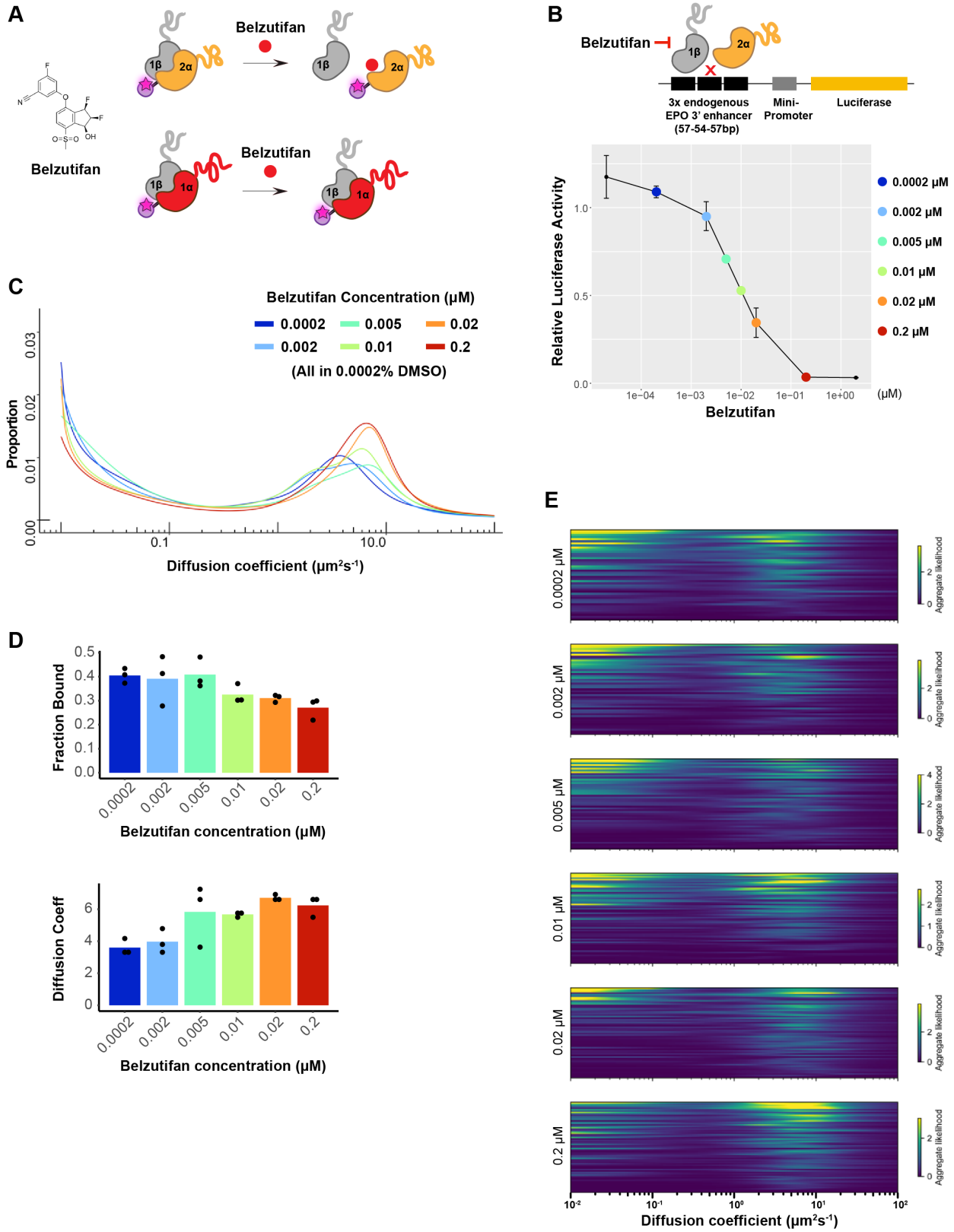

1318 **Figure 3—figure supplement 1.** Dosage-dependent inhibition of HIF-2α binding and activity by

1319 Belzutifan. (**A**) Molecular structure of Belzutifan (PT-2977) and schematic illustration of its function
1320 to specifically block dimerization between HIF-2α/1β but not HIF-1α/1β. (**B**) Luciferase assay
1321 using an HRE-containing reporter confirms Belzutifan dosage-dependent inhibition of HIF-2α
1322 activity in WT 786-O cells. Error bars represent SE. (**C**) Proportion of molecules as a function of
1323 diffusion coefficient for HIF-2α measured in Halo-HIF-2α KIN line clone A31 treated with different
1324 concentrations of Belzutifan. DMSO levels are kept the same for all conditions at 0.0002%. (**D**)
1325 The average fraction bound decreases (top) and the average peak position diffusion coefficient
1326 increases (bottom) at increasing doses of Belzutifan. Individual measurements are indicated as
1327 black dots. (**E**) RBME likelihood of diffusion coefficient in individual cells for all six drug dosages.

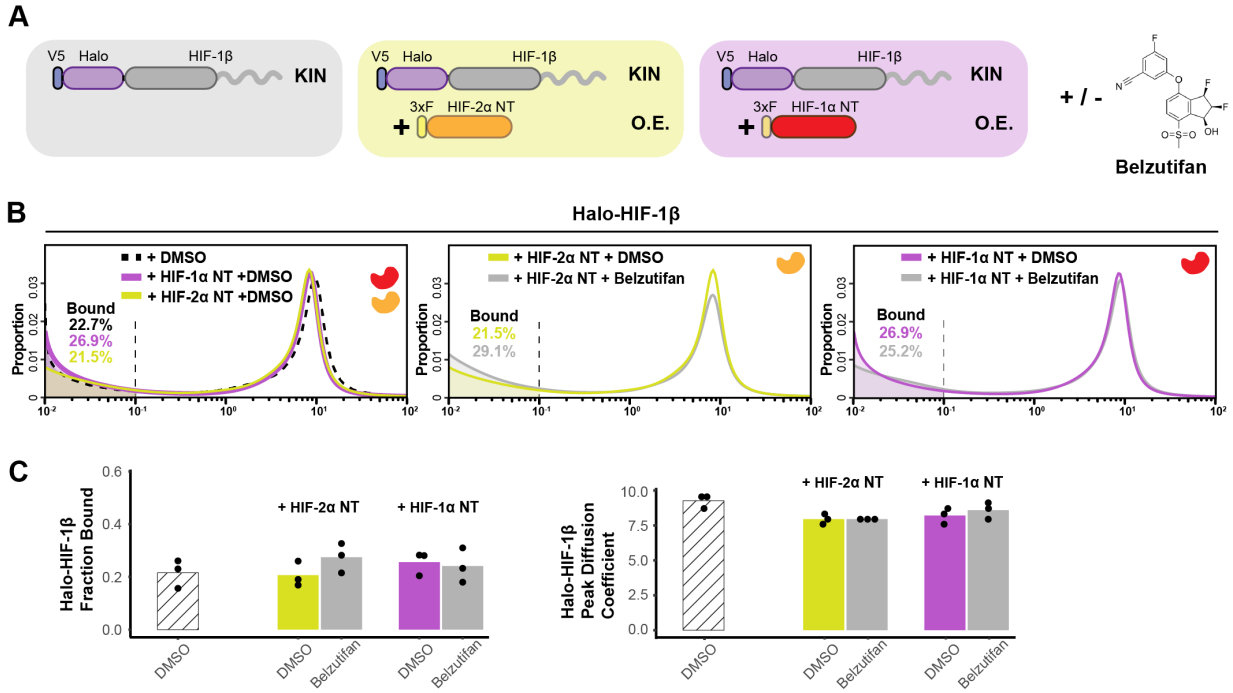

Figure 3—figure supplement 2. Additional data for Figure 3 showing HIF-α without the IDR is not able to increase HIF-1β binding or decrease its diffusion coefficient (**A**) Schematic of evaluating Halo-HIF-1β behavior while overexpressing only the N-terminal structured region (NT) of HIF-α in combination with small molecule perturbation. Parental Halo-HIF-1β KIN cells (grey background, same as in Figure 3) and cells stably overexpressing (O.E.) either HIF-2α NT (orange in yellow background) or HIF-1α NT (red in purple background) are used, with and without treatment with 0.2-μM Belzutifan. (**B**) Proportion of HIF-1β molecules as a function of diffusion coefficient measured in various cells outlined in (A). Left: treated with DMSO only, comparing HIF-1β behavior in the parental cells (black dashed curve, same as in Figure 3) and in cells expressing either HIF-1α NT (purple curve) or HIF-2α NT (yellow curve). Middle and right: proportions of HIF-1β as a function of diffusion coefficient, measured in cells expressing either HIF-1α NT (right) or HIF-2α NT (middle) with Belzutifan treatment (grey curves), compared to the DMSO control (purple or yellow curves). (**C**) Summary of the average bound fractions (left) and peak diffusion coefficient (right) for conditions in (B), with black dots indicating values from each of the three individual measurements.

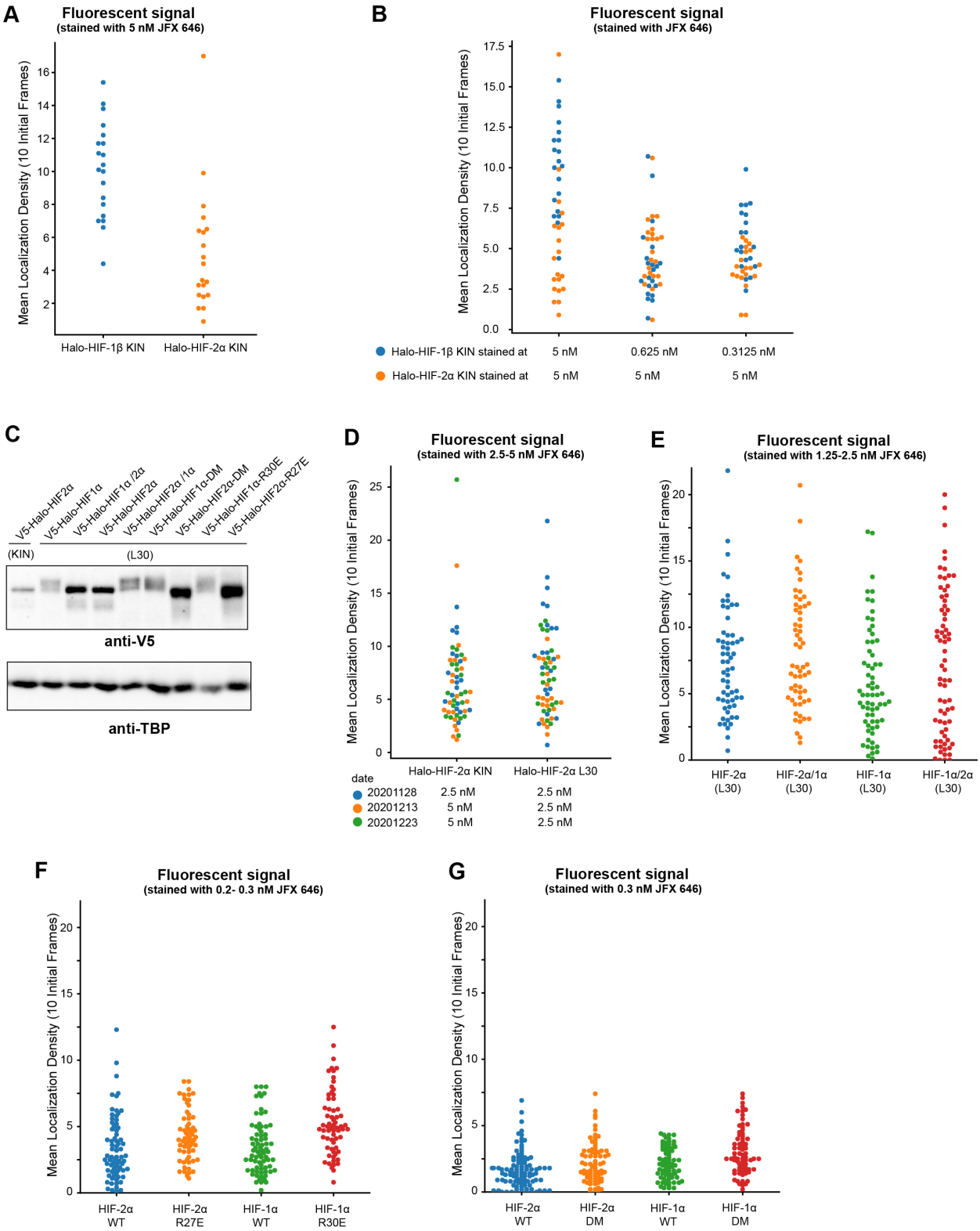

1344 **Figure 4—figure supplement 1.** Quantification of initial localization density showing we imaged
1345 cells with similar expression levels of Halo-tagged proteins. (**A**) When cells were stained with

1346 the same dye concentration, a much higher mean density of fluorescence spots at the first 10
1347 frames (i. e. initial localization density) was observed for proteins with higher expression levels.
1348 (**B**) In order to achieve a similar initial localization density, a much lower dye concentration has
1349 to be used (~1/10 of concentration used for Halo-HIF-2α is needed for Halo-HIF-1β). When a
1350 similar dye concentration is used (0.625 and 0.3125 nM), the initial localization density for the
1351 same protein (Halo-HIF-1β) looks similar. (**C**) Western blot analysis of expression level of
1352 various Halo-tagged proteins in KIN cells and in cells with L30-expression system. Bulk results
1353 are mixed-population average and do not reflect expression levels from individual cells. (**D-G**)
1354 Analysis of initial localization density for data used in Figure 4—figure supplement 2 (D), Figure
1355 4 (E), and Figure 5 (F and G) showing similar initial localization density for all cells imaged for
1356 each set of experiments, verifying comparable expression levels across the samples.

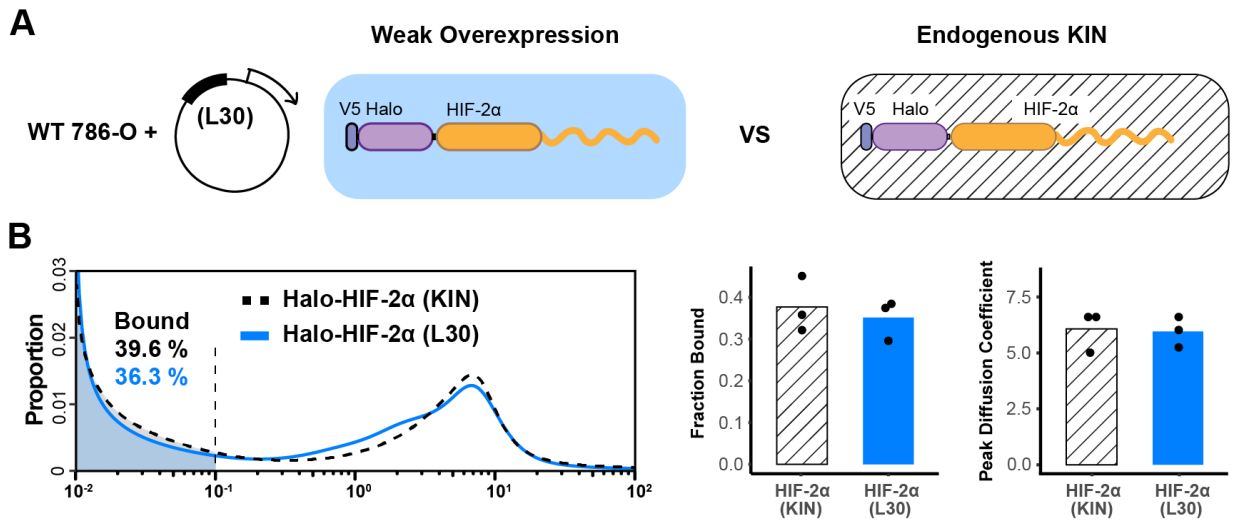

Figure 4—figure supplement 2. L30 weak expression system is able to recapitulate the endogenous protein behavior. **(A)** Schematic of the L30 overexpression system where Halo-HIF-2α is weakly expressed with an L30 promoter in wild-type 786-O cells (left) and Knock-in cells where HIF-2α is endogenously tagged and expressed (right). **(B)** Comparison between endogenous Halo-HIF-2α (KIN) and Halo-HIF-2α over-expressed with L30 promoter (L30), showing very similar behavior. Left: Proportion of Halo-HIF-2α as a function of diffusion coefficient and the corresponding bound fraction (shaded area). Right: Bar plot summarize the average bound fraction (left) and peak diffusion coefficient (right) with three independent measurements (black dots).

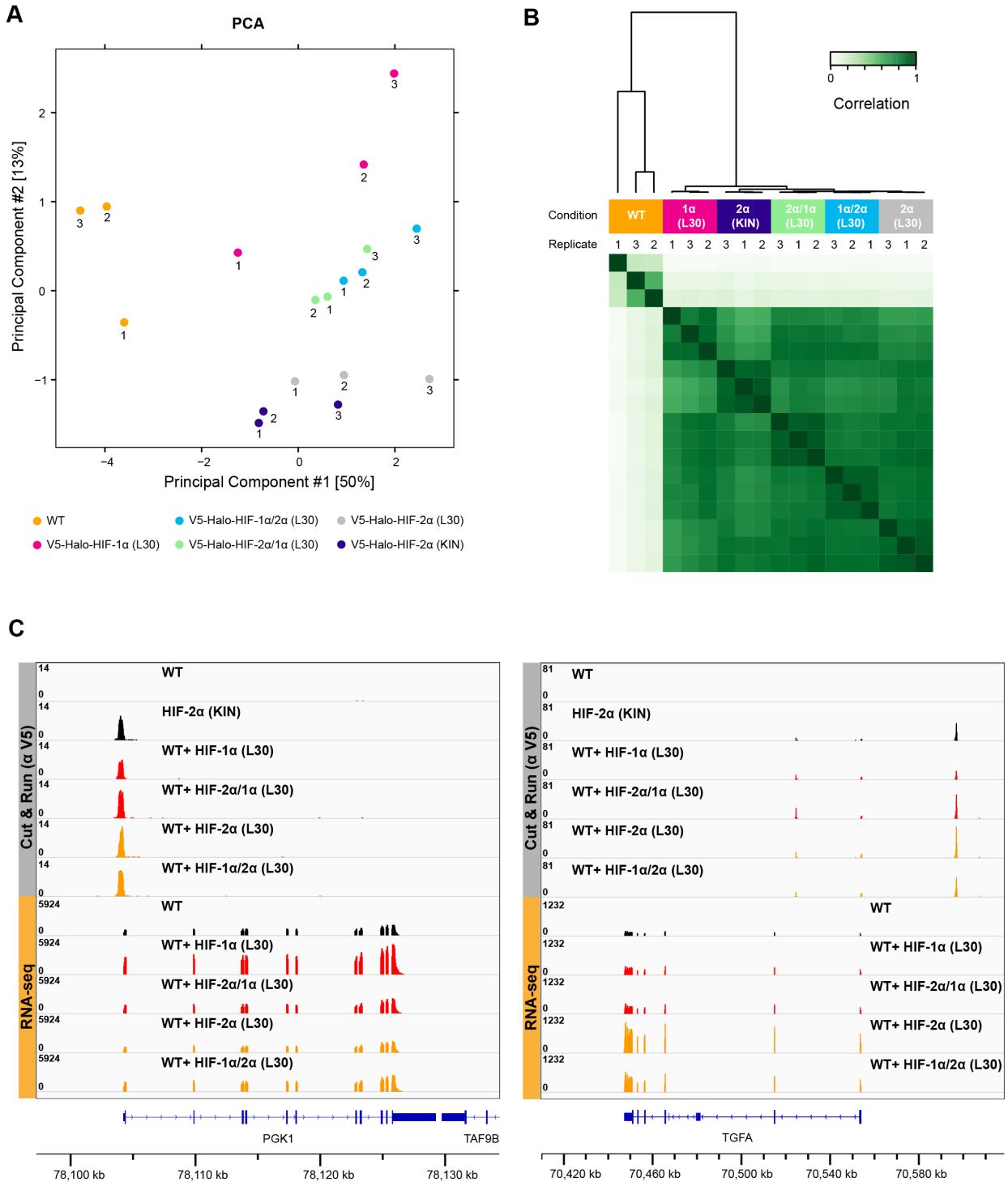

Figure 6—figure supplement 1. Cut&Run results show no difference in overall binding profiles between different HIF-α variants. (**A-B**) PCA (A) and clustering (B) analysis of anti-V5 Cut&Run results performed on WT 786-O cells, Halo-HIF-1α KIN clone A31, and WT cells expressing Halo-tagged HIF-α variant (-1α, -2α, -2α/1α, or -1α/2α) with L30 promoter. Except for WT

1370 control, all L30-driven HIF-α variants have very similar and close to endogenous HIF-2α binding
1371 profile. (**C**) Two examples of genome browser views of Cut&Run results showing all four HIF-α
1372 variants bind to the same sites with similar strength, even when the target genes are only
1373 upregulated by overexpression HIF-α (left, PGK-1) or HIF-2α (right, TGFA).

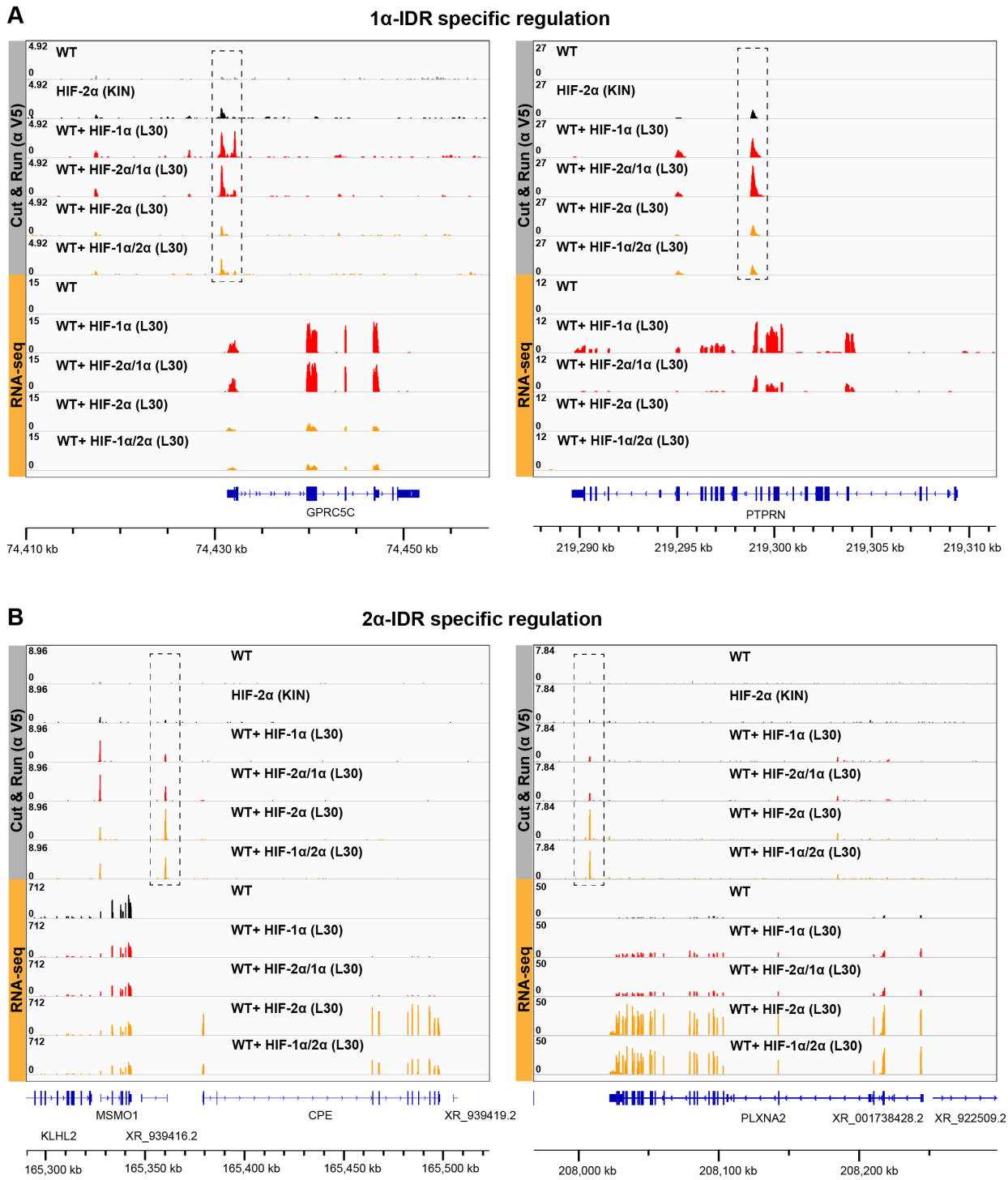

Figure 6—figure supplement 2. Additional examples showing that HIF-α IDR contributes to isoform-specific chromatin binding preferences. (**A**) two additional examples of genes that are activated by HIF-1α and -2α/1α overexpression, and also have elevated binding by HIF-1α and -2α/1α at regulatory sites (dashed boxes) (**B**) two additional examples of genes that are

1378 activated by HIF-2α and -1α/2α overexpression, and also have elevated binding by HIF-2α and -
1379 1α/2α at regulatory sites (dashed boxes).

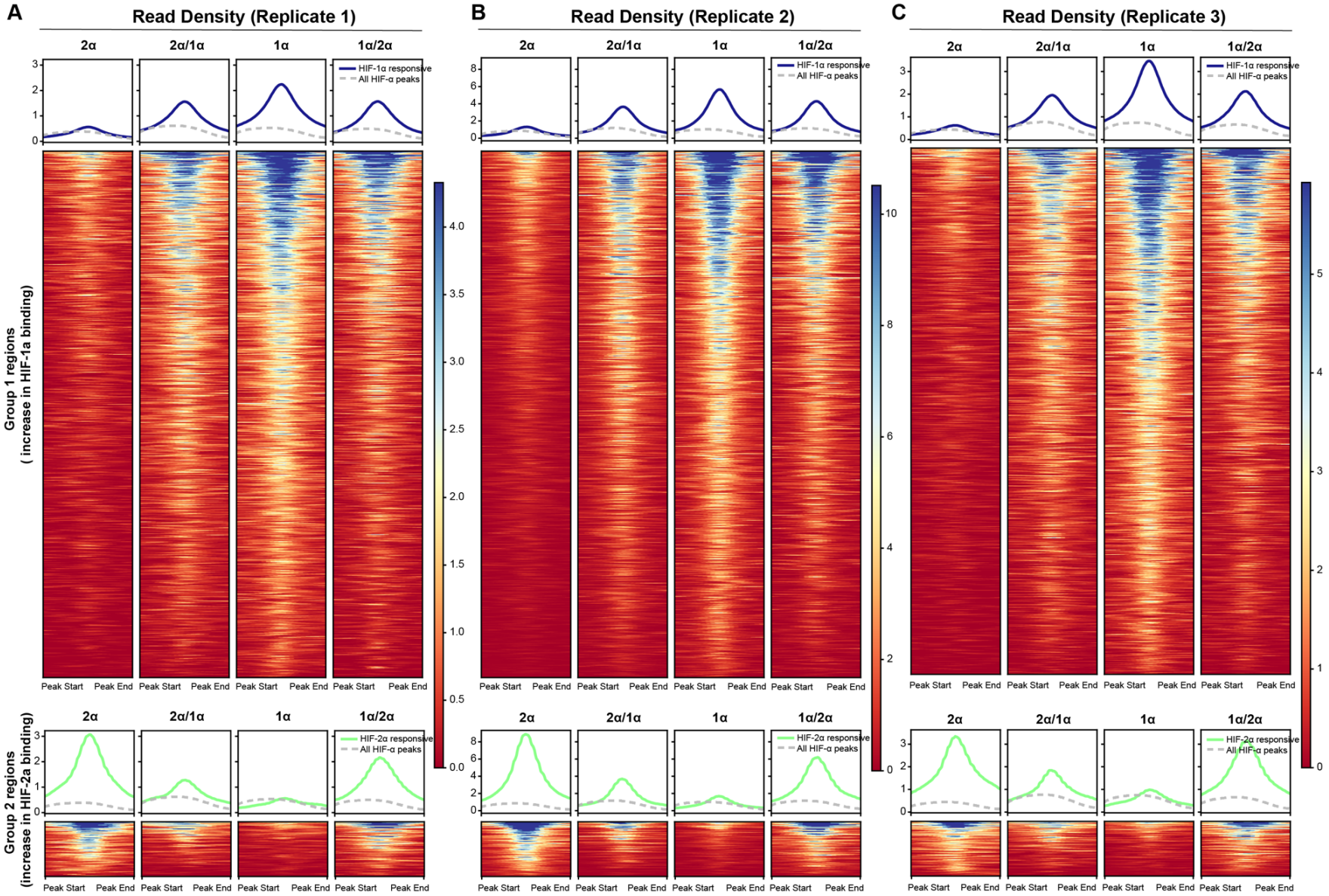
A
Read Density (Replicate 1)
B
Read Density (Replicate 2)
C
Read Density (Replicate 3)
2α
2α/1α
1α
1α/2α
HIF-1α responsive
All HIF-α peaks
HIF-2α responsive
All HIF-α peaks
Group 1 regions
(increase in HIF-1a binding)
Group 2 regions
(increase in HIF-2a binding)
Peak Start
Peak End

1380

1381 **Figure 6—figure supplement 3.** Results from analyzing Cut&Run individual replicates showing
1382 reproducibility (**A-C**) Same analyses as for the combined replicates in Figure 6C were performed
1383 for Cut&Run individual replicates.

1384 **Table 4.** Constructs used to generate stable cell lines
1385

Name	Prom-oter	Gene product	Short name in the paper	Appeared in
PB EF1a 3XF EX-MCS IRES Puro	EF1a	3xFLAG tag	3xF	Figure 3
PB EF1a 3XF-GDGAGLIN-hEPAS1 IRES Puro	EF1a	HIF-2α N-terminally fused with 3xFLAG tag through a short peptide linker sequence (GDGAGLIN)	HIF-2α	Figure 2 Figure 3 Figure 2—figure supplement 2
PB EF1a 3XF-GDGAGLIN-hEPAS1_R171A-V192D IRES Puro	EF1a	HIF-2α dimerization mutant (R171A-V192D) N-terminally fused with 3xFLAG tag through a short peptide linker sequence (GDGAGLIN)	HIF-2α DM	Figure 2 Figure 2—figure supplement 2
PB EF1a 3XF-EPAS1_365 IRES Puro	EF1a	The N terminal region of HIF-2α (aa 1-365) N-terminally fused with 3xFLAG tag	HIF-2α NT	Figure 3—figure supplement 2
PB EF1a 3XF-EPAS1_365-364_HIF1a IRES Puro	EF1a	HIF-2α/1α chimera protein (aa 1-365 of HIF-2α and aa 364-826 of HIF-1α) N-terminally fused with 3xFLAG tag	HIF-2α/1α	Figure 3
PB EF1a 3XF-GDGAGLIN-hHIF1a IRES Puro	EF1a	HIF-1α N-terminally fused with 3xFLAG tag through a short peptide linker sequence (GDGAGLIN)	HIF-1α	Figure 3
PB EF1a 3XF-HIF1a_363 IRES Puro	EF1a	The N terminal region of HIF-1α (aa 1-363) N-terminally fused with 3xFLAG tag	HIF-1α NT	Figure 3—figure supplement 2
PB EF1a 3XF-HIF1a_363-366_EPAS1 IRES Puro	EF1a	HIF-1α/2α chimera protein (aa 1-363 of HIF-1α and aa 366-870 of HIF-2α) N-terminally fused with 3xFLAG tag	HIF-1α/2α	Figure 3
PB L30prom V5-Halo-GDGAGLIN-hEPAS1 IRES Puro	L30	HIF-2α N-terminally fused with V5-HaloTag through a short peptide linker sequence (GDGAGLIN)	Halo-HIF-2α (L30)	Figure 4 Figure 4—figure supplement 2
PB L30prom V5-Halo-GDGAGLIN-hEPAS1_365-364_HIF1a IRES Puro	L30	HIF-2α/1α chimera protein (aa 1-365 of HIF-2α and aa 364-826 of HIF-1α) N-terminally fused with V5-HaloTag through a short peptide linker sequence (GDGAGLIN).	Halo-HIF-2α/1α (L30)	Figure 4
PB L30prom V5-Halo-GDGAGLIN-hHIF1a IRES Puro	L30	HIF-1α N-terminally fused with V5-HaloTag through a short peptide linker sequence (GDGAGLIN)	Halo-HIF-1α (L30)	Figure 4
I_PB L30prom V5-Halo-GDGAGLIN-HIF1A_363-366_EPAS1 IRES Puro	L30	HIF-1α/2α chimera protein (aa 1-363 of HIF-1α and aa 366-870 of HIF-2α) N-terminally fused with V5-HaloTag through a short peptide linker sequence (GDGAGLIN).	Halo-HIF-1α/2α (L30)	Figure 4
PB L30prom V5-Halo-GDGAGLIN-hEPAS1 IRES Puro_R27E	L30	HIF-2α DBD mutant (R27E) N-terminally fused with V5-HaloTag through a short peptide linker sequence (GDGAGLIN).	Halo-HIF-2α, R27E (L30)	Figure 5
PB L30prom V5-Halo-GDGAGLIN-hHIF1a IRES Puro_R30E	L30	HIF-1α DBD mutant (R30E) N-terminally fused with V5-HaloTag	Halo-HIF-1α, R30E (L30)	Figure 5

		through a short peptide linker sequence (GDGAGLIN).		
PB L30prom V5-Halo-GDGAGLIN-hEPAS1_R171A-V192D IRES Puro	L30	HIF-2α dimerization mutant (R171A-V192D) N-terminally fused with V5-HaloTag through a short peptide linker sequence (GDGAGLIN).	Halo-HIF-2α DM (L30)	Figure 5
PB L30prom V5-Halo-GDGAGLIN-hHIF1a_R170A-V191D IRES Puro	L30	HIF-1α dimerization mutant (R170A-V191D) N-terminally fused with V5-HaloTag through a short peptide linker sequence (GDGAGLIN).	Halo-HIF-1α DM (L30)	Figure 5

1386
1387

1388 **Appendix 1. Analysis of source of variations.**
1389 Since we observed huge cell-to-cell variation (Figure 2A-B), we used bootstrapping to determine
1390 the source of variation, and decide how many cells, replicates and trajectories will be needed to
1391 get a relatively good estimate for the parameters.
1392
1393 We used Halo-HIF-2α KIN clone A31 for the bootstrapping, as this is the cell line where the
1394 most data were collected. We used 243 movies (each movie corresponds to one cell) collected
1395 from 11 different replicates (each replicate was done on a different day) as the pool to draw
1396 sample from. We performed sampling in three different ways. First, we pooled all trajectories
1397 from all cells and randomly drawn different number of trajectories (i.e. sample size n= 10, 25,
1398 50, 100, 200, 400, 800, 1600, 3200 and 6400) from the pool with replacement. After each draw,
1399 the resulting trajectories were used for SA analysis to generate the diffusion spectrum and then
1400 the fraction bound was calculated. We performed 100 draws for each of the sampling size and
1401 plotted box plot on the resulting bound fraction estimation to see variation. This way, we can
1402 estimate if we randomly sample n trajectories 100 times, how variable the result will be. The
1403 result was as expected- the more trajectories we draw, the less variable the estimation is
1404 between the 100 times of drawing when looking at the bound fraction (Figure 2—figure
1405 supplement 3A, left).
1406
1407 Second, instead of sampling a mixture of trajectories from all 243 cells, we randomly picked N
1408 number of unique cells (N = 1, 10, 20, 40, 60, 80, 100, 120) from the 243 cells, pooled the
1409 trajectories from these selected cells, and sampled from these pooled trajectories. The sample
1410 size and number of draws were kept the same. This way, we can compare if we randomly take
1411 only N cells from the population (243 cells) to estimate the bound fraction, do that 100 times for
1412 each sample size, how bad the variation is compared to if we take all 243 cells. This will be a
1413 good estimation of how many cells we need to pick. Certainly, small number of cells gives
1414 smaller number of total trajectories and if we draw large number of trajectories from them (such
1415 as n = 6400) it will be over-sampled. Our result shows that when we pick as many as 60 cells,
1416 the difference of estimated bound fraction from these 60 cells compared to when estimated from
1417 all 243 cells can be less than 5% when sampling more than 800 trajectories (Figure 2—figure
1418 supplement 3A, middle; and 3B).
1419
1420 Third, since different replicates were performed on different days, we use day as the unit to
1421 group trajectories. We randomly picked 1 day (i.e. 1 replicate), combined all trajectories from

1422 Halo-HIF-2α KIN clone A31 from that day, which normally is ~20 cells, and use this mixture of
1423 trajectories for sampling. This way, we can compare how variable our estimation will be from
1424 replicate to replicate. Indeed 1 replicate is not good enough to give good estimation as the
1425 variation is still high even if we sample large number of trajectories (Figure 2—figure
1426 supplement 3A, right). However, if we randomly pick 3 days instead of 1, we reduce the
1427 variance, and the estimated bound fraction from these 3 days compared to when estimated from
1428 all 243 cells from 11 days can be less than 5% when sampling more than 800 trajectories
1429 (Figure 2—figure supplement 3C).
1430
1431 From our bootstrapping results, we think an estimation of bound fraction from 3 replicates with
1432 20 cells each replicate (and usually we can collect total more than 2500 trajectories from 3
1433 replicates) can be good enough, at least for comparing different conditions such as WT versus
1434 mutants, where a difference of 10% bound fraction was usually observed.

1435 **Appendix 2. Using fluorescence intensity as approximation for protein expression level.**
1436 Since we have shown that stoichiometry may affect protein behavior, to compare the molecular
1437 dynamics across different HIF-α forms that were exogenously expressed, it is important to
1438 control for similar expression levels. Unfortunately, we observed variegated expression levels
1439 with the same L30 promoter even with stable cell lines. As a result, for exogenously expressed
1440 Halo-proteins in Figure 4 and Figure 5, we used fluorescence intensity as approximation for
1441 protein expression levels to guide our selection of which cell to image.
1442
1443 During imaging, cells were doubly labeled- one channel with excess JFX549 dye (500 nM),
1444 which was used for localizing cells and define ROI, the other channel with limited JFX646 dye
1445 for fSPT (Figure 1D). The expression level for the Halo-tagged protein can be estimated by
1446 either looking at fluorescence intensity from the JFX549 channel, or looking at the initial
1447 localization density (i.e. average number of molecules detected per ROI) from the JFX646
1448 channel. For quantification of initial localization density, we only averaged the first 10 frames of
1449 each movie, because the initial frames have minimum impact from photobleaching.
1450
1451 For Halo-HIF-1β and Halo-HIF-2α KIN lines, because the endogenous HIF-1β expresses at a
1452 much higher concentration than HIF-2α, when cells were fully labelled with JFX549, the
1453 fluorescence level for Halo-HIF-1β KIN cells were much higher than Halo-HIF-2α KIN cells.
1454 Similarly, when stained with same concentration of JFX646 for these two cell lines, the overall
1455 Halo-HIF-1β localization density was much higher compared to Halo-HIF-2α, consistent with
1456 much higher expression levels (Figure 4—figure supplement 1A). However, for SPT, a low
1457 localization density is needed to minimize tracking error. To keep localization density low, for
1458 Figure 2, Halo-HIF-1β had to be stained at ~1/10 of the JFX646 concentration used for Halo-
1459 HIF-2α (Figure 4—figure supplement 1B, 0.3125 or 0.625 nM instead of 5 nM) to achieve ideal
1460 localization density that is similar to Halo-HIF-2α (orange dots). This shows that for different
1461 expression levels, an order-of-magnitude difference in dye concentration needs to be used to
1462 get similar localization density. In addition, we found that while 5 nM gives very high localization
1463 density, when stained at a similarly low concentration (0.3125 vs 0.625 nM), the resulting
1464 localization density for Halo-HIF-1β was also roughly the same. This shows that with similar dye
1465 concentration, localization density can be a rough approximation for protein levels.
1466
1467 We then utilize the localization density as a quality control for experiments where expression
1468 level needs to be kept similarly. For the L30 driven Halo-HIF-α expression, the variation of

1469 expression level is big from cell to cell and we are able to find cells with similar expression
1470 levels (close to endogenous) across different HIF-α variants. Thus, we used the JFX549
1471 channel to pick cells with similar fluorescence intensity (usually the lowest intensity, which is the
1472 closest to endogenous expression level) for imaging, after cells were fully labeled with JFX549.
1473 Because these cells were also stained with similar level of JFX646 dye for fSPT when a set of
1474 experiments with multiple conditions were compared, cells picked for similar JFX 549 intensity
1475 usually have similar localization densities in the JFX 646 channel. As confirmed by
1476 quantification in Figure 4—figure supplement 1D-G, we did have very close localization density
1477 for different conditions in each set of experiments performed, indicating that for each
1478 comparison, the expression level across different conditions were kept roughly similar.